PHYSICAL REVIEW FLUIDS **8**, 120501 (2023)

Invited Articles

Floating wind farm experiments through scaling for wake characterization, power extraction, and turbine dynamics

Juliaan Bossuyt,[1] Ondřej Ferčák,[1] Zein Sadek,[1] Charles Meneveau,[2]
Dennice F. Gayme,[2] and Raúl Bayoán Cal[1,*]
[1]*Department of Mechanical and Materials Engineering, Portland State University, Portland, Oregon, USA*
[2]*Department of Mechanical Engineering, Johns Hopkins University, Baltimore, Maryland 21218, USA*

(Received 1 July 2023; accepted 13 October 2023; published 14 December 2023)

In this study, wind and water tunnel experiments of turbulent wakes in a scaled floating wind farm are performed. Scaling of a floating wind farm with a scaling ratio of 1:400 is made possible by relaxing geometric scaling of the turbine platform system, such that the dynamic response can be correctly matched, and to allow for relaxing Froude scaling such that the Reynolds number can be kept large enough. Four dimensionless parameters, describing the relative importance of wind and wave loads compared to turbine inertia, are used to guide the scaled floater design. Free decay tests of the pitch and heave response confirm that the dimensionless natural frequency of the scaled model is in the typical range for full-scale floating turbines when matching the proposed four dimensionless parameters. The response and performance of a single turbine scaled model are characterized for different wind and wave conditions. Subsequently, a wind farm experiment is performed with twelve floating turbine models, organized in four rows and three columns. Particle image velocimetry measurements of the wake of the middle turbine in the third row reveal distinct differences in wake properties for different wave conditions. Conditional averaging confirms a synchronization of wake deflection with the traveling waves in the wind farm. The power outputs show distinct peaks at the wave frequencies and its harmonics, due to motions triggered by complex wave-turbine-wake interactions. The power spectrum of the aggregate power of three streamwise aligned turbines exhibits anticorrelation of motions at the wave frequency due to wave speed induced phase lag, and spatiotemporal correlations of power outputs at the frequency corresponding to the wind-convective time between two rows. These experiments using an appropriately scaled floating wind farm in a wind tunnel setup confirm distinct impacts of turbine motion on wake recovery and meandering, and measurement results highlight the intricate interactions between wave topology and wake meandering.

DOI: 10.1103/PhysRevFluids.8.120501

I. INTRODUCTION

The vast wind energy potential above deep ocean waters has motivated increasing government investment in the development of floating wind plants. At the end of 2022, 15 GW of floating wind capacity was auctioned on the U.S. west coast, to be installed by 2035 [1]. A total of 23 GW floating wind capacity is planned in Scottish waters, of which 18 GW was auctioned in 2022 [2], and Portugal increased its goal for floating wind energy with an aim to auction 10 GW of capacity in 2023 [3]. The world's first commercial floating wind farm, the 30 MW Hywind in Scotland, has hit record high power capacity factors [2]. Estimates show that there is significant potential to reduce

---

[*] Corresponding author: rcal@pdx.edu

costs as indicated by the U.S. Department of Energy's plans to reduce costs of floating wind by 70% by 2035 [4]. However, a better understanding of the complex interactions between different types of ocean waves and turbulent winds is needed to further improve turbine and platform designs and robustness, as well as to reduce the cost of floating wind energy. The associated improvements to system reliability and lower costs are imperative for floating wind to play a significant role in helping to respond to the global demands to transition to renewable energy sources.

Platform stability and unsteady loading are two main topics early studies have focused on to enable floating wind technology [5–8]. Advanced water basin tests, with Froude-scaled floating wind turbines have allowed for accurate quantification of dynamic response to incoming wave and wind conditions [5]. The results have been essential for the validation of numerical simulations of floating wind turbine dynamics. Froude scaling is required for scaled experiments to simulate the hydrodynamic response to the incoming wave field correctly [9]. Froude scaling focuses on the ratio of flow momentum to gravitational forces and is a proven approach for scaling hydrodynamic experiments. However, Reynolds number scaling requires higher wind speeds than Froude scaling and is therefore very difficult to be satisfied simultaneously. As a result, Froude-scaled tests are challenged in reproducing realistic thrust and power coefficients [10]. The topic of several studies has, therefore, been to develop solutions to simulate wind forces, for example, by using low-Reynolds number rotors, porous disks, ducted fans, or propellers to generate representative thrust [10]. The Reynolds number is an important limitation of Froude-scaled tests, typically limiting the scaling ratios to be on the order of 1:50. As a result, Froude-scaled models typically have a rotor diameter on the order of 2 m or larger. Due to these large rotor diameters, combined with challenges in generating realistic aerodynamic performances, Froude-scaled tests make it very challenging to study the impact of turbine motion on wake characteristics especially in typical wind tunnel facilities for which test sections much larger than 2 m would be required (i.e., to produce precisely controlled wind conditions and measurements, as opposed to open water basin tests with external fans).

To overcome these challenges, research has focused on wake properties of static misaligned rotors [11–18] and rotors subject to oscillating motions, such as pitch, heave, and surge [19–26], without considering the hydrodynamic two-way coupling with wave motions. Messmer *et al.* [25] provides a recent overview and discussion of wake behavior for moving rotors. By prescribing actuated rotor motions, experiments can ensure aerodynamic scaling of wake properties more easily. Simulations [19,27–35] and experimental studies [20,36–45] have shown a strong sensitivity of wake properties to the dynamic motion of a wind turbine rotor. Depending on the dimensionless frequency of the rotor motion, or Strouhal number ($\mathrm{St} = fD/U_h$, with f being the frequency of motion, D the rotor diameter, and U_h the inflow wind speed at hub height), wake recovery can be accelerated. Especially for higher Strouhal numbers, an amplification of the wake meandering amplitude has been observed, leading to nonlinear wake dynamics and faster wake recovery [25]. A differentiation can be made between slow rotor motions (e.g., $\mathrm{St} < 0.05$) leading to wake deflection and displacement, and faster motions (e.g., $\mathrm{St} > 0.2$) [25,40], leading to this amplification of wake meandering amplitude and nonlinear wake dynamics. Both operating zones need to be studied, given the large range of timescales describing the motion of a floating wind turbine.

Due to wake spreading, turbine power in the fully developed region of large wind farms becomes governed by vertical transport of mean kinetic energy from the high momentum flow above [46–58]. Therefore, it is important to study the impact of floating turbine motions on wake recovery in a wind farm setting, where turbines are subject to wake turbulence from many upstream turbines. Yang *et al.* [59] performed large eddy simulations (LES) of a fixed bottom offshore wind farm exposed to long-period ocean waves, as well as shorter-period localized wind-driven waves. Those LES results indicate the importance of considering the wave-wind-turbine coupling in studying the wake characteristics and available power. More specifically, it was found that long-period swell waves can increase the downwards transfer of mean kinetic energy in a fully developed wind farm array. More recently, Ferčak *et al.* [60] performed wind tunnel tests of a fixed bottom wind turbine subject to long-period swell waves. In that work wave topology was also found to impact the wake recovery

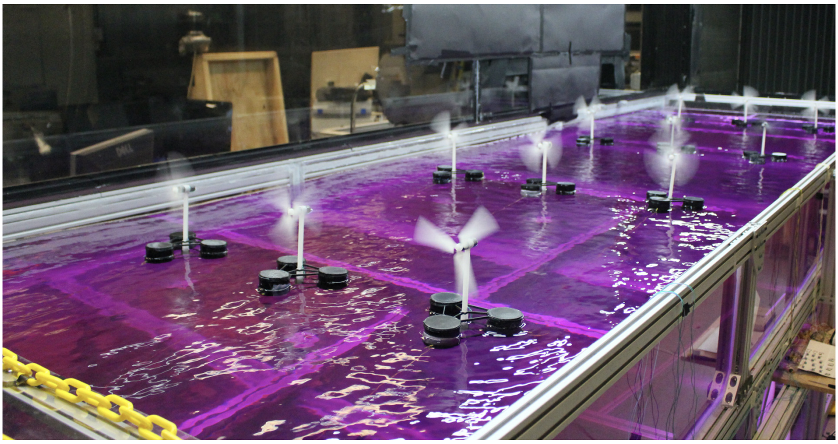

FIG. 1. Photograph of the scaled floating wind farm setup in the Portland State University wind and water tunnel.

and velocity profile to heights as high as the turbine tip height. An LES study by Yang *et al.* [61] showed that lateral swell waves can cause wake deflection, due to the locally induced change in wind direction.

It is evident that floating turbine wakes can be influenced by wave conditions and rotor motions, thus leading to a complex turbine-wind-wave coupling. In a floating wind farm, this interaction can extend over groups of turbines as the turbine/platform motion and wakes affect each other. Such couplings can lead to not only improved (or reduced) power output, but also to power fluctuations at dominant frequencies related to the farm layout, the wind, and wave conditions. There is a need for experimental data of such wind-wave-wake-turbine interactions in a floating wind farm, for validation and to study in more detail the underlying mechanisms. However, due to the practical testing limitations described above, most wind tunnel studies of floating wind turbine wakes have focused on prescribing the rotor motion while using a fixed wind tunnel floor (i.e., without a free surface and waves), thus ignoring dynamic wave-turbine interactions.

Here, a scaling methodology for floating wind farm experiments using laboratory wind and water tunnel setups is presented, as shown in Fig. 1. The proposed scaling method strikes a balance between the desirability of matching different dimensionless groups (Reynolds number, Froude number, Strouhal numbers, thrust coefficient, tip speed ratio, etc.), and practical restrictions which inevitably mean that not all of these groups can be matched simultaneously for the large scale ratios required (typically 1:200 to 1:1000 and above). In analogy with the use of low-Reynolds number airfoil profiles (i.e., a change of rotor geometry) for scaled turbine models that enables to relax the matching of the Reynolds numbers, an approach in which floater geometry designs are changed to reproduce the correct dynamic response and enable to relax matching the Froude numbers is proposed. Floaters are designed in a manner that improves the turbine/platform hydrodynamic response. Specifically, a small-scale floating wind turbine model is introduced, that is designed to approximate full-scale turbine motions, as characterized by appropriately redefined Strouhal numbers and scaled motion-amplitudes. Based on typical offshore weather, and the dominant factors determining floating turbine motion, conditions with long period swell waves and high wind speed are selected. By combining turbine power, turbine motion, wave topology, and wake measurements, the aim is to reproduce the dominant features of wind loads, wave fields, and platform motion, their interactions and effects on wake behavior and wind farm performance.

Following a discussion of the scaling methodology in Sec. II, the measurement techniques are documented in Sec. III. In Sec. IV the experimental setup, the scaled floating turbine, wind farm, and wave conditions are presented. Section V presents the measured performance of a single floating turbine. In Sec. VI, the wake, motion, and power measurements of the scaled floating wind farm are presented and discussed.

II. SCALING METHODOLOGY

Offshore wind turbines have a diameter that typically ranges from about 60 to 120 m, becoming increasingly larger with new developments. Conversely, a scaled turbine model for wind farm experiments in a typical wind tunnel, requires rotor diameters on the order of 0.1–0.3 m [13,62–64]. The corresponding required geometrical scaling ratios are thus typically between 1:200 to 1:1200, making the scaling very challenging.

One of the main challenges for performing scaled experiments of floating bodies is scaling the aerodynamic and hydrodynamic (interactions with the free surface) conditions simultaneously, one requiring similarity of Reynolds number ($\mathrm{Re}_D = U_h D/\nu$), tip speed ratio ($\mathrm{TSR} = \omega R/U_h$), thrust coefficient ($C_T = 2F_{\mathrm{WT}}/\rho U_h^2 A$), power coefficient ($C_p = 2P/\rho U_h^3 A$), and Strouhal number of rotor motions ($\mathrm{St} = fD/U_h$), while the other mainly requiring Froude number scaling ($\mathrm{Fr} = U_h/\sqrt{gD}$). In these equations, U_h is the incoming mean wind speed at hub height, D the turbine diameter, ν the kinematic viscosity of air, ω the angular speed of the rotor, A the cross-sectional area of the rotor, ρ the density of the fluid, f the frequency of the motion, and g the gravitational acceleration.

The Froude number is relevant for flows in which the inertial forces occur together with gravitational forces, and thus for free surface flows in general [65]. Froude number scaling can also become important for matching the relative inertia of an object when studying the interaction with wind loading and the resulting dynamic motion. This requirement is discussed specifically for a floating turbine below.

If the same medium is used for scaled tests, air and water in this case, then only one dynamic scaling ratio can be fulfilled simultaneously [66]. For example, given a typical rotor mass on the order of 100,000 kg or more, and a rated wind speed of 12 m/s for a 5 MW wind turbine [67], a Froude-scaled turbine with a scaling ratio of 1:600 should have a rotor mass of 0.0005 kg, and would have to be tested with a wind tunnel speed of 0.5 m/s. It is not possible to build a working 0.5 g model turbine and the Reynolds number would be too small to reproduce realistic wake properties.

Therefore, in typical scaled tests of coastal processes length-scale ratios are typically limited to about 1:50 [68], and Reynolds similarity is almost always relaxed, as gravitational forces are predominant in free-surface flows [65].

For floating wind turbine applications, the effects of Reynolds number have to be taken into account, even if perfect similarity (matching Reynolds numbers) cannot be enforced. Given this, it is not possible to match Reynolds numbers with a model turbine [69] (using the same fluid at standard atmospheric conditions, a length-scale ratio of 600 would imply that one needs to run the wind tunnel at speeds 600 times that of wind, i.e., hypersonic speeds). If the same rotor geometry would be used in scaled wind tunnel tests at lower Reynolds numbers, then the reduced lift generated by the blades due to the much lower Reynolds number would result in an unrealistically small power coefficient, thrust coefficient, and tip speed ratio [62,70,71]. To circumvent this challenge, experimental wind tunnel studies use airfoil profiles more suitable for low Reynolds numbers, and with larger chord lengths to reproduce realistic full-scale lift coefficient, as visualized in Fig. 2(b). This approach is well established for wind tunnel testing of wind farms [13,60,62,64,72,73], and though the Reynolds number is not matched, the main properties of turbine wakes in turbulent boundary layers can be captured as long as the model Reynolds number is held above a critical Reynolds number, $\mathrm{Re}_D > 2\text{–}4.8\times10^4$ [63,72,74]. This is an example of a scaling approach in which geometric similarity is relaxed (e.g., blade profile), to better match the essential dimensionless parameters for wake properties (thrust coefficient, power coefficient, and tip speed ratio).

Similarly, for scaled tests of a floating wind turbine with a scaling ratio in the range of 1:200 to 1:1000, exact Froude scaling is impossible even if the Reynolds number is not matched and is only kept high enough above the critical value needed ($\mathrm{Re}_D > \mathrm{Re}_{D,\mathrm{crit}}$) as described before. As a result of not following Froude number scaling, the scaled model will have a relatively larger inertia

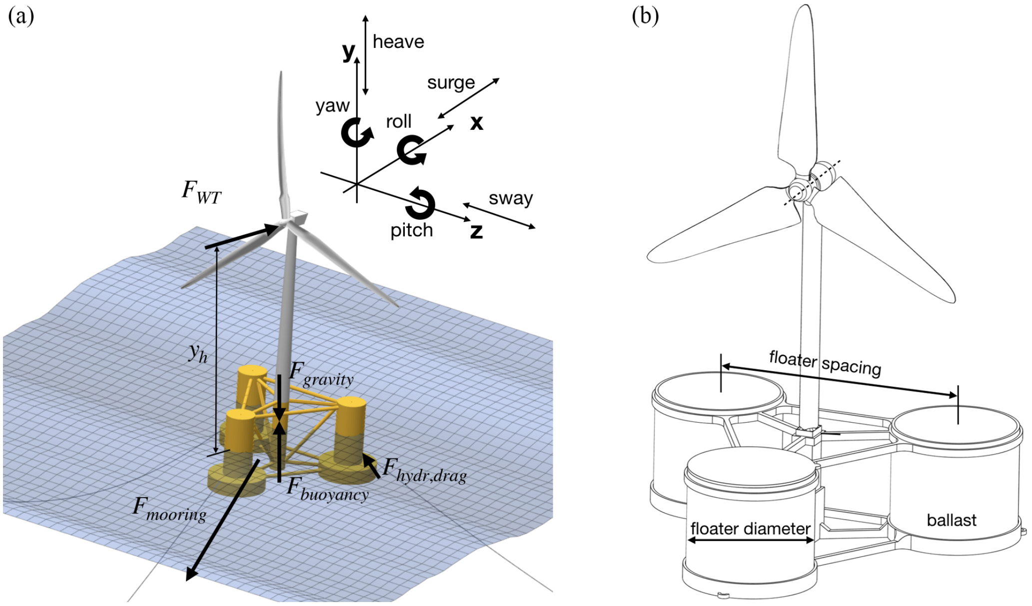

FIG. 2. A schematic representation of several forces acting on a floating turbine, represented on the OC5 DeepCWind turbine with NREL 5 MW rotor as visualized in QBlade [76] (a), and a schematic representation of floater design parameters that can be altered to improve the response of a small-scale model (b).

compared to the external loads, thus affecting its response to wind and wave loads. Therefore, the approach followed in this paper considers a redesign of the floating structure to match the important dimensionless numbers for wake properties; the Strouhal number and dimensionless measures of the amplitude of the six degrees of freedom (i.e., sway, heave, surge, pitch, yaw, and roll as indicated in Fig. 2).

In practice, the motions of a floating turbine are strongly determined by its natural frequencies [5,75]. Therefore, the dimensionless natural frequencies (i.e., as a Strouhal number) need to be matched as closely as possible. A floating turbine can be approximated by a harmonic oscillator with external loading (e.g., wind, waves, and elastic mooring forces). To match the natural frequency for a scaled model that is relatively heavier due to not matching Froude scaling, the hydraulic restoring force and moment can be altered by changing the floater design.

The motion of a floating turbine is described by the balance of all forces $\vec{F}_i$ and moments $\vec{M}_i$ in each direction (Newton's second law for translation and rotation), as

$$\sum \vec{F}_i = m\vec{a}, \tag{1}$$

and

$$\sum \vec{M}_i = \mathbf{I}\vec{\alpha}, \tag{2}$$

leading to one equation for each motion (sway, heave, surge, roll, pitch, and yaw). Here, m is the mass of the entire turbine, $\vec{a}$ the acceleration, $\mathbf{I}$ the rotational mass moment of inertia, and α the angular acceleration, implicitly including the effects of added mass, hydrostatic forces, damping, and external forces. Figure 2(a) presents a schematic representation of different forces acting on a real floating wind turbine. For a floating wind turbine the wind force is mainly balanced by inertia of the turbine and structure, floater drag loads, buoyancy forces generated by the floaters, and mooring forces. The floater drag loads have a component due to frictional losses and form-drag losses. (Reproducing the full-scale conditions, water surface tension effects need to be negligible in the model as well.) To scale the motion of a floating turbine, it is thus important that the relative contribution of each term in Eqs. (1) and (2) is similar. Therefore, several ratios of forces and moments are considered next, to scale the relative impact of wind and wave loads on the motion of a floating turbine. Four main dimensionless ratios of interest are selected for this study.

The relevant scale for acceleration is chosen as $a_0 = U_h^2/D$, with U_h the incoming hub wind speed, and D the rotor diameter. The scale for angular acceleration is chosen as $\alpha_0 = \Delta\theta U_h^2/D^2$, with $\Delta\theta = 1\text{deg}$ chosen arbitrarily, but not affecting the comparison between full-scale and scaled model given the objective of similar angular displacement for kinematic similarity.

The ratio of wind-thrust-force F_{WT} to turbine inertia ma_0 represents the sensitivity of surge turbine acceleration to wind load fluctuations:

$$R1 = \frac{F_{\text{WT}}}{ma_0}, \tag{3}$$

with

$$F_{\text{WT}} = \tfrac{1}{2}\rho_{\text{air}}U_h^2AC_T, \tag{4}$$

ρ_{air} the density of air, and A the rotor area. Using the relation for wind thrust and acceleration scale, the ratio reduces to $R1 = 1/8\rho_{\text{air}}\pi D^3C_T/m$. Keeping this ratio constant for a scaled model, and given that we do not want to change C_T to preserve correct wake properties, the mass needs to scale with D^3, which is the same requirement as for Froude scaling [77].

The ratio of heave response force $\Delta F_{\text{hydr},\Delta h}$ to turbine inertia ma_0, characterizes the responsiveness of the floating structure to incoming waves or heave motions in general. Considering the geometric scaling of wave conditions and wind turbine size, the ratio is calculated for submerging the turbine with a fixed depth scaled by turbine diameter $\Delta h = D$. The ratio is written as

$$R2 = \frac{\Delta F_{\text{hydr},\Delta h}}{ma_0}, \tag{5}$$

with

$$\Delta F_{\text{hydr},\Delta h} = \rho_{\text{water}}A_{\text{platform}}Dg. \tag{6}$$

In this equation, ρ_{water} is the density of water, and A_{platform} the total floater cross-sectional area at the water surface. Thus, $R2 = (\rho_{\text{water}}A_{\text{platform}}D^2g)/(mU_h^2)$, giving a relation for the cross-sectional area of the floating platform as a function of the geometric scaling, the ratio of wind speeds, and the ratio of mass. If the analogy is made with a harmonic oscillator description of a floating turbine, then this ratio of a spring force to turbine mass reflects the scaling of the squared dimensionless natural frequency to heave motions. By manipulating the cross-sectional area of the model, the aim is to match R2 between full-scale and model conditions as well as possible.

For pitching motions, the moment generated by the wind-thrust force M_{WT} is compared to the rotational inertia of the floating turbine for pitch $I_z\alpha_0$. This ratio represents the sensitivity of the pitching motion of the turbine to wind velocity fluctuations:

$$R3 = \frac{M_{\text{WT}}}{I_z\alpha_0}, \tag{7}$$

with

$$M_{\text{WT}} = y_hF_{\text{WT}}, \tag{8}$$

and using D as a scale for y_h, resulting in:

$$R3 = \frac{1}{8}\frac{\rho_{\text{air}}\pi C_T}{\Delta\theta}\frac{D^5}{I_z}. \tag{9}$$

It is also desirable to match R3 as closely as possible. Similarly as for ratio R1, since the wind speed and turbine diameter are used as a scaling for time, velocity, and acceleration, the only way to match R3 is by scaling the mass moment of inertia with D^5 (unless a reduction in $\Delta\theta$ is acceptable), which corresponds to the same requirement as for Froude scaling [77]. Technically, there is an opportunity to change the design such that the mass moment of inertia scales with D^5, though this would counteract the requirements for ratio R2 and R4. Inevitably, the rotational inertia of the scaled turbine to wind fluctuations will be relatively higher, so that only the large-scale velocity fluctuations will have an effect on pitch angle. Contrary to R1, the moment generated by the wind loads can be significant compared to rotational inertia for a full-scale floating turbine (e.g., $R3 \approx 0.6$ as estimated for the OC5 DeepCWind floating wind turbine design [75]). However, this ratio does not fully describe the turbine response to wind fluctuations, as other loads also play a role (e.g., the hydraulic floater restoring moment, the rotor gyroscopic inertia, among others). It is important to note that ratio R3 does not relate to the magnitude of pitch motions due to steady wind loads, but instead to the relative inertia of the turbine (i.e., the inertia of the turbine acts as a low pass filter to wind load fluctuations, such that for a smaller value of R3, the motion will mostly be governed by the slower changes in wind loads).

The ratio of the hydraulic pitch restoring moment $M_{\Delta\theta}$ to the rotational inertia $I_z\alpha_0$ indicates the responsiveness of the floating wind turbine to incoming waves. A higher ratio will correspond to a higher natural frequency for pitching. The ratio is written as

$$R4 = \frac{M_{\Delta\theta}}{I_z\alpha_0}. \tag{10}$$

The R4 ratio needs to be calculated for a specific change in pitch angle, which is arbitrarily chosen as $\Delta\theta = 1\mathrm{deg}$, as it will not impact the comparison between full-scale and model-scale. For a semisubmersible design, one can aim to match this ratio by changing the diameter and spacing of the floaters, thereby increasing the hydraulic restoring moment for pitch.

III. MEASUREMENT TECHNIQUES

This section details the used measurement techniques. Particle image velocimetry (PIV) is used for wake measurements, light-induced fluoresence (LIF) is used to measure the water height and wave properties, and a stereo-camera setup is used to optically track the motion of a floating turbine. The measurements make reference to an experimental setup (described in more detail later in Sec. IV) in a closed-loop wind tunnel with a floor consisting of a water tank with wave paddle and wave damper. Single or arrays of floating wind turbine models are placed on the water surface. A standard PIV measurement setup is used, which is detailed in Appendix A.

A. Light induced fluorescence measurement of water interface

The transient water surface profile is measured using LIF [78]. A setup with a FLIR BFS-U3-51S5M camera, a 532 nm optical filter, a 200 mW (532 nm) continuous LED laser sheet, and a commercially available red fluorescent dye, is used to characterize the waves. A cropped region of interest is acquired using the camera sensor to cover only the region where the water height is visible, enabling a sampling rate increase to 250 Hz. Figure 3 shows an example of a recorded image for wave shape identification. Using standard image processing techniques, based on light intensity, the wave height is deduced from each image. The wave period is found from the frequency spectrum of wave height at a fixed location, and the wave velocity from the time lag corresponding to the maximum correlation between wave height time signals at two points with maximum separation in the field of view. The uncertainty of the wave speed is estimated from the sampling frequency (± 0.01 s), distance between the two points, and the measured velocity itself. The wavelength λ and its uncertainty are derived from the measured wave period T and wave velocity V, according to $\lambda = VT$. The estimated uncertainty on wave speed and wave length is $\pm 5\%$. See Sec. IV B for more detail about the measured conditions.

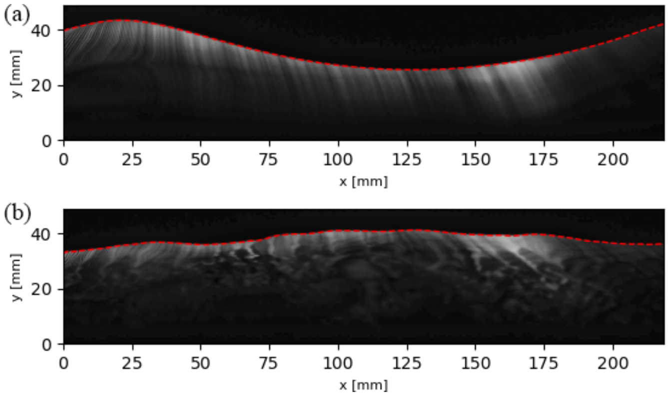

FIG. 3. Example of images used for water surface measurements. Standard computer vision algorithms are used to identify the air-water interface, as indicated by the red-dashed line. Panel (a) is for a wave frequency of 2.7 Hz with no wind, while panel (b) is for a wave frequency of 1.5 Hz and a wind speed of 5.4 m/s.

B. Optical tracking of floating wind turbine

The motion of the floating turbine is measured with a stereo-camera setup, using two FLIR BFS-U3-16S2C-CS cameras, with a 1.6 MP resolution and a maximum frame rate of 226 fps. Camera calibration and 3D reconstruction using line-of-sight is done following the polynomial fitting approach by Machicoane *et al.* [79]. A calibration plate is accurately positioned in increments of 10 mm with a traversing system and captured by the camera setup in the wind tunnel. Both cameras are synchronized with an external trigger signal at a frequency of 200 Hz, generated by an Arduino microcontroller. Each camera is connected to a dedicated workstation to retrieve and save the frames. Checkerboard markers are placed on the floating turbine and rotor, using decal paper. The markers are tracked using a combination of OpenCV tools in Python and a custom prediction step for the subsequent marker locations. The best accuracy of the marker positions is found using a cross-correlation approach of the marker region with an ideal saddle point pattern, and fitting a 2D polynomial to the cross-correlation values to retrieve the location of the maximum value with subpixel accuracy. Given that the angular position changes of the floating turbine are not large, there is no need to include a rotational dependence for the saddle point cross-correlation. A series of high-power LED flood lights are used, powered by a DC power supply, to enable a small exposure time for the cameras with global-shutter, as to freeze the motion of the turbine blades. The error on reconstructing the calibration points is within $\pm$ 0.5 mm. On one turbine, 13 chessboard marker points are tracked on the tower, and one chessboard marker point on each floater. Figure 4 shows the tracked markers on a floating turbine model, with a visualization of the measured marker motion. Knowing the relative positions of the marker points, from a calibration in standstill, the motion of the turbine is found from fitting the set of reference marker locations to the measured locations using a minimization algorithm, giving the six degrees of freedom: yaw, roll, pitch, heave, surge, and sway.

IV. EXPERIMENTAL SETUP

The closed-loop wind tunnel at Portland State University (PSU) has a test section with length 5 m, width 1.2 m, and height 0.8 m. A schematic representation of the wind tunnel test section, with wave paddle, wave damper, and floating wind turbines is shown in Fig. 5. The wind tunnel speed can range from 2 to 40 ms^{-1}, and the ceiling is configured to approach a zero-pressure gradient boundary layer during the experiments. The sidewalls are assembled of Schlieren-grade annealed float glass fastened to the steel framework to ensure maximum optical access for the laser and

FIG. 4. Camera snapshot used for optical tracking, with indication of tracked markers and their previous trajectory for an incoming hub wind speed of 2.9 m/s and 1.2 Hz wave conditions.

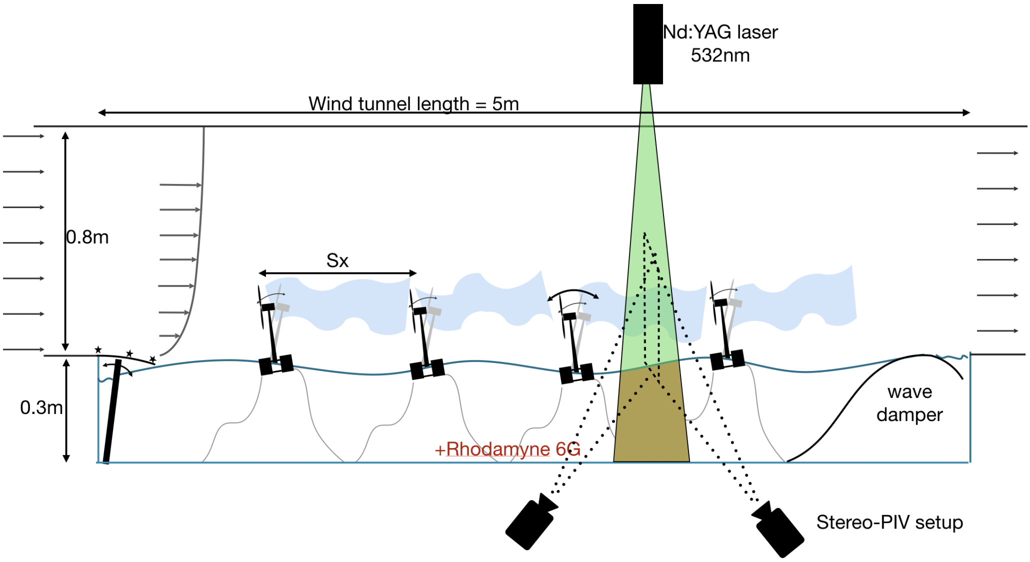

FIG. 5. Schematic representation of the measurement setup in the Portland State University wind tunnel.

camera [80–82]. An expansion-contraction section with mesh in the low-speed zone reduces the background turbulence intensity at the inlet. For the present experiments, no turbulence grid is used, resulting in a uniform low-turbulence inflow. The floor of the wind tunnel test section is replaced by a water tank with wave paddle and wave damper, as described in more detail in Sec. IV B. A photograph of the scaled floating wind farm in the wind tunnel test section is shown in Fig. 1. In the following sections, the floating wind turbine model design and wave conditions are described.

A. Floating wind turbine

The rotor design by Odemark and Fransson [83] is used and geometrically scaled from a diameter of $D = 0.226$ m to a diameter of $D = 0.15$ m. The rotor is 3D printed on a 3D Systems ProJet MJP 3600 in high detail resin. The same rotor and size has already been used successfully in a previous wind tunnel study of a scaled fixed bottom offshore wind turbine [60]. A Faulhaber 1331T012SR direct current (DC) motor, with a diameter of 13 mm is used as a DC generator to control the tip speed ratio. The maximum power coefficient is found for a tip speed ratio of TSR = 5 (see Sec. V). The power coefficient is estimated to be $C_P \approx 0.25$, using the measured current and the motor torque constant specified by the manufacturer, which gives a rough estimate following the discussion by Bastankhah and Porté-Agel [64]. The TSR is controlled using a variable resistor to maximize the power coefficient. Thin 30 AWG silicone flexible electric wires are used to connect the DC generator of the floating turbine to a 200 Ohm variable resistor outside of the wind tunnel, as to minimize impact on motion due to wire stiffness. The rotor thrust coefficient is estimated to be $C_T \approx 0.65$ by measuring the turbine thrust force with a miniature double-beam load cell, and for the turbine in a fixed, nonfloating position [60]. As desired, the power coefficient is a good approximation of full-scale conditions (although still being somewhat smaller).

There are many different floater designs for floating wind turbines considered in the literature, and every design has its own characteristics and optimal use-cases. In this study the choice was made to scale a semisubmersible design, which has generally a stronger pitch response to incoming wave slope changes, and a motion which is more determined by the floater geometry instead of mainly the mooring stiffness. Furthermore, the semisubmersible DeepCWind design is well documented in the literature, and provides a useful reference for our experiments.

The most challenging part is matching the kinematic response of a full-scale floating wind turbine, as determined mainly by the natural frequency (Strouhal number) of the turbine, and motion amplitudes. In this first scaling attempt, the objective is to design a model turbine matching the response of a full-scale floating turbine with a diameter of 60 m, thus requiring a scaling ratio of 1:400. High wind speed conditions are considered, with a hub wind speed of 25 m/s (close to its maximum limit). The floating platform of the OC5 DeepCwind turbine [75] is used as a reference for the 60m diameter rotor. Because the mass of the rotor and tower represents only 3% of the total mass, the OC5 DeepCwind floater properties (such as total mass, and mass moment of inertia) are not adjusted for the smaller rotor diameter, and the information documented by Robertson *et al.* [75] is used.

As discussed in Sec. II, a minimum wind speed is required for the wind tunnel tests to have a sufficiently high Reynolds number for wake properties. To ensure a Reynolds number well above 20 000, we chose to operate the tunnel at a wind speed such that the hub wind speed inside the wind farm is around 2.9 m/s. Naturally at this small value, the Froude number cannot be matched with the full-scale system. To match Froude numbers, one would require a velocity ratio equal to $400^{1/2} = 20$, i.e., a wind tunnel speed less than 1 m/s which then implies a Reynolds number significantly below the desired threshold value of 20 000. A scaled model turbine is needed which can operate in higher wind speeds than required by strict Froude scaling (without capsizing), yet has a representative dynamic response to wind and wave loads. Also, the higher wind speed and structural and material challenges, inevitably results in a scaled model that is heavier than required by Froude scaling. Considering the force and moment ratios R1–R4 discussed in Sec. II, the floater diameter (D_{floaters}) and floater spacing (L) are increased to improve the response of the scaled model.

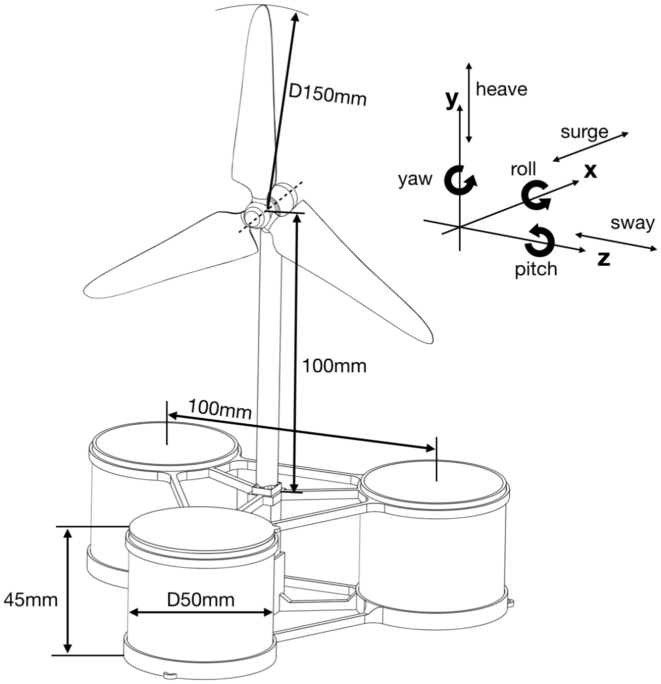

FIG. 6. Schematic of scaled-down floating wind turbine model with key dimensions.

The main objective is to match the natural frequency and amplitudes for pitch, roll and heave motions to those of a full-scale turbine, as closely as possible. See Appendix B for an illustration of the sensitivity of the pitch natural frequency to ballast weight and floater dimensions for a number of different floater designs. After iterating multiple designs, a final design was selected based on the measured natural frequencies, 3D-printing constraints, and wind tunnel size limitations. The final dimensions arrived at in the present study are shown in Fig. 6. The corresponding weight distribution and mass moment of inertia, as calculated by the CAD software are documented in Table I.

The scaling ratios as described in Sec. II are compared between the scaled model and the full-scale target turbine (OC5 DeepCWind platform + 60m diameter rotor) in Table II. Despite the very large scaling ratio of 1:400, the ratios R1 to R4 are matched reasonably well, with average ratio of

TABLE I. Geometric properties of the scaled-down model.

Rotor diameter	0.15 m
Hub height above water line	0.113 m
Total mass	164 g
Mass rotor	4 g
Mass DC generator	19 g
Mass of tower + electric wires	16 g
Mass of floater w/o ballast	56 g
Mass of ballast	69 g
Floater diameter	0.05 m
Floater spacing	0.1 m
Mass moment of inertia for pitch	6.73×10^{-4} kgm^2

TABLE II. Overview of scaling parameters compared to a reference floating wind turbine with a rotor diameter of 60 m and fixed to the OC5 DeepCWind platform.

	Full-scale reference	Laboratory-scale model	$\frac{\text{Full-scale}}{\text{Laboratory-scale}}$
Rotor diameter [m]	60	0.15	
Wind speed [m/s]	25	2.9	
CT	0.65	0.65	
Hub height [m]	43	0.113	
Total mass [kg]	1.4×10^{7}	0.16	
Hydrostatic restoring moment in pitch [Nm/rad]	-1.4×10^{9}	-9.6×10^{-2}	
Hydrostatic restoring moment in heave [N/m]	3.8×10^{6}	58	
Mass moment of inertia for pitch [kgm^2]	1.6×10^{10}	6.7×10^{-4}	
R1	0.005	0.006	0.8
R2	1.6	0.9	1.7
R3	0.016	0.035	0.4
R4	0.009	0.007	1.3

ratios of order unity. It is thus expected that this scaled model will have a similar responsiveness to wind and wave loads for surge, heave and pitch motions.

The natural frequency for pitch, roll and heave were measured from the free-decay impulse response with optical tracking, as shown in Fig. 7. Table III presents the measured natural frequency of the scaled model. The measured frequencies are also scaled to full-scale conditions, using the estimated hub-height velocity in the wind farm experiment $U_h = 2.9\,\text{m/s}$ (see Sec. VI), and the rotor diameter $D = 0.15$ m. As a reference, we mention that the pitch natural frequency of full scale semisubmersible floating wind turbines is typically in the range of 0.02–0.06 Hz [84–90], and is 0.035 Hz for the OC5 DeepCWind turbine with NREL 5 MW rotor [75]. Scaled to a full-scale turbine with diameter of 60 m and for a hub wind speed of 25 m/s, the model natural frequency is around 0.032 Hz, and thus matches the typical range very well. Similarly, the measured heave natural frequency scaled to reference turbine conditions corresponds to 0.054 Hz, in agreement with the natural frequency of 0.057 Hz for the OC5 DeepCWind turbine with an NREL 5 MW turbine [75]. The Strouhal number corresponding to the pitch natural frequency of a full-scale turbine (i.e., a natural frequency of 0.035 Hz for turbines with $D = 60$ m up to $D = 120$ m and $U_h = 6$ m/s up to $U_h = 30$ m/s) can range from $\text{St} = 0.07$ up to $\text{St} = 0.7$. The pitch natural frequency Strouhal number of the scaled model $\text{St} = 0.08$ matches well compared to the reference turbine with $D = 60$ m, $U_h = 25$ m/s, and a natural frequency of 0.035 Hz, leading to $\text{St} = 0.08$. If we extend the scaling to the OC5 DeepCWind turbine with an 126 m NREL 5 MW rotor, then the corresponding natural frequency is 0.015 Hz for pitch, which is a factor 2 smaller. Thus, for a larger

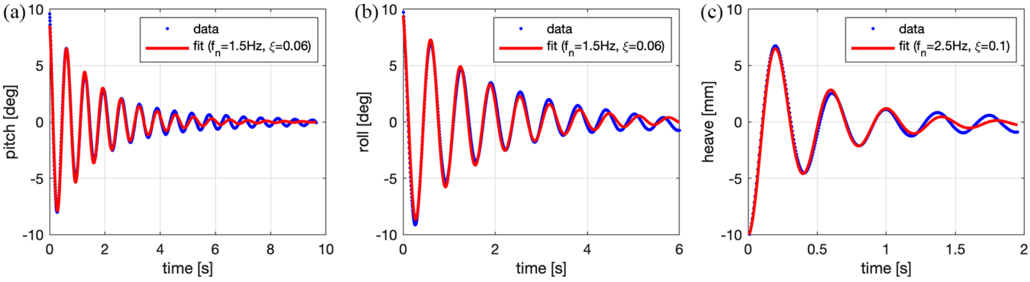

FIG. 7. Optical measurement of impulse response with no-wind for tilt (a), roll (b), and heave (c).

TABLE III. Measured natural frequency for pitch, heave, and roll, from fitting the impulse response to free-decay tests.

Free decay response	Measured natural frequency model [Hz]	Scaled to $D = 60$ m $U_h = 25\,\text{m/s}$ [Hz]	Scaled to $D = 126$ m $U_h = 25\,\text{m/s}$ [Hz]	Strouhal number	Damping ratio
Pitch	1.5	0.032	0.015	0.08	0.06
Roll	1.5	0.032	0.015	0.08	0.06
Heave	2.5	0.054	0.026	0.13	0.1

rotor diameter than the target of 60m, some further adjustments to the floater design should be made. For reference, Table IV presents a comparison of the dimensionless ratios with the OC5 DeepCWind turbine with NREL 5 MW rotor. In this case the R1 to R4 ratios are larger, indicating the relatively higher dimensionless inertia. As a result, compared to this larger turbine, the scaled model will have less sensitivity to smaller wind fluctuations, while the dominant motions will be mostly triggered at a Strouhal natural frequency which is a factor 2 smaller. The ratios R2 and R4 represent the ratio of a dimensionless spring constant (hydrostatic restoring force or moment) over inertia (mass for R2, mass moment of inertia for R4). Making the analogy with a harmonic oscillator, the square root of these ratios links to the dimensionless natural frequency of the turbine $f_n = \sqrt{k/m}$, with k the spring constant and m the mass. The square root of the ratio of R4 is 2.4, which corresponds with the ratio of the OC5 DeepCwind + NREL 5 MW natural frequency divided by the measured scaled natural frequency for pitch, i.e., 0.035 Hz/0.015 Hz $\approx$ 2.3.

In general, we conclude that by adjusting the floater design it is possible to bring the response of a scaled model closer to that of a full-scale floating turbine. As discussed in Sec. V, for wind-only, no-wave conditions, the measurements show pitch fluctuations of $\pm 2^o$ around the mean, showing that the wind-driven pitch fluctuations have a similar magnitude as for full-scale turbines [91].

Floating turbines are connected to the seabed with a mooring system. Scaling the mooring system is challenging as it can strongly affect the motion of the turbine under wind and wave loading. A simple three line mooring system is used to keep the floating turbines in place, see Fig. 8 for the configuration using thin nylon braided wires. Optimizing the design of a scaled mooring system for

TABLE IV. Overview of scaling parameters compared to a reference floating wind turbine with an NREL5MW rotor fixed to the OC5 DeepCWind platform.

	Full-scale reference	Laboratory-scale model	$\frac{\text{Full-scale}}{\text{Laboratory-scale}}$
Rotor diameter [m]	126	0.15	
Wind speed [m/s]	25	2.9	
CT	0.65	0.65	
Hub height [m]	90	0.113	
Total mass [kg]	1.4×10^7	0.16	
Hydrostatic restoring moment in pitch [Nm/rad]	-1.4×10^9	-9.6×10^{-2}	
Hydrostatic restoring moment in heave [N/m]	3.8×10^6	58	
Mass moment of inertia for pitch [kgm^2]	1.6×10^{10}	6.7×10^{-4}	
R1	0.045	0.006	7.0
R2	7.0	0.9	7.4
R3	0.64	0.035	18.1
R4	0.040	0.007	5.9

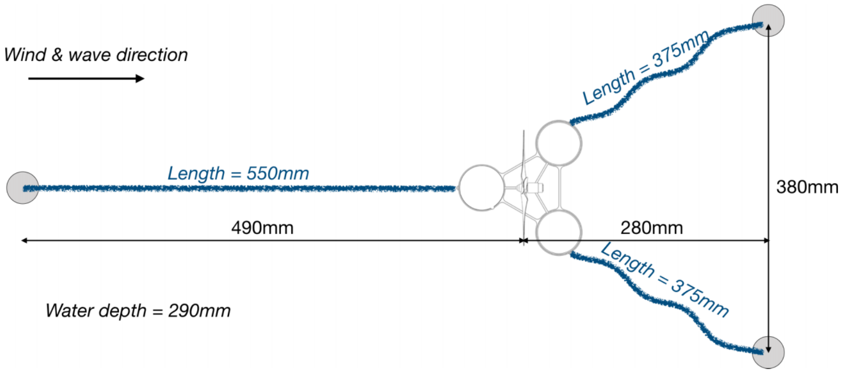

FIG. 8. Schematic of the mooring setup.

a floating wind turbine experiment is left for future studies, and no scaling effort is done to match the stiffness of the mooring system at this time. The resulting motion of the moored floating turbines is measured for each condition and discussed in Sec. V.

B. Wave conditions

The focus of this study is on long period ocean waves, which have a wave period closer to the natural frequency for pitch and roll of a full-scale floating turbine (e.g., ocean swell waves with a period ranging from 15 to 20+ s, as compared to a typical system period for pitch and roll of 33 s, and 17.5 s for heave [75]). As opposed to local wind-driven waves, long period waves present a more idealized test condition and can be generated with a precisely controlled wave paddle. Small-scale wave interactions, such as small waves created by the floater motion, and effects of water material properties such as surface tension are, therefore, not critical to match in this experiment. In this study, wave conditions are tested with a frequency below, close to, and faster than the natural frequency of the model for pitch.

As shown in Fig. 5, an oscillating wave paddle is used to generate waves in the water tank. The wave paddle is located at the entrance of the wind tunnel test section, such that the waves move in the same direction as the wind. The wave paddle is actuated by a stepper motor, of which the rotational speed can be controlled. Via 3D printed cams, the amplitude of the wave paddle can be adjusted, though only one setting is used in this study for all waves. At the end of the wind tunnel test section a wave damper is located. The water depth is set to 0.29 m such that the waves just partly roll over the wave damper, resulting in minimal reflections. Leftover wave energy gets trapped behind the wave damper where it dissipates.

The wave parameters are measured using LIF (see Sec. III A) for different frequencies of the wave paddle, corresponding to different wave periods, and for no-wind conditions. Figure 9 shows

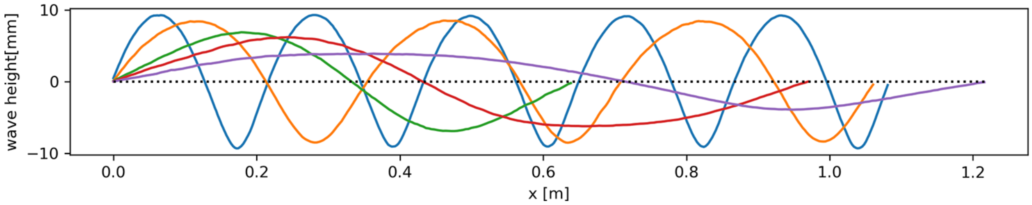

FIG. 9. Measured wave shapes for no-wind condition, projected to spatial coordinates using the measured wave velocity. The wave shapes are shown for 2.7, 2.0, 1.5, 1.2, and 1 Hz waves, in order from smallest to largest wave length.

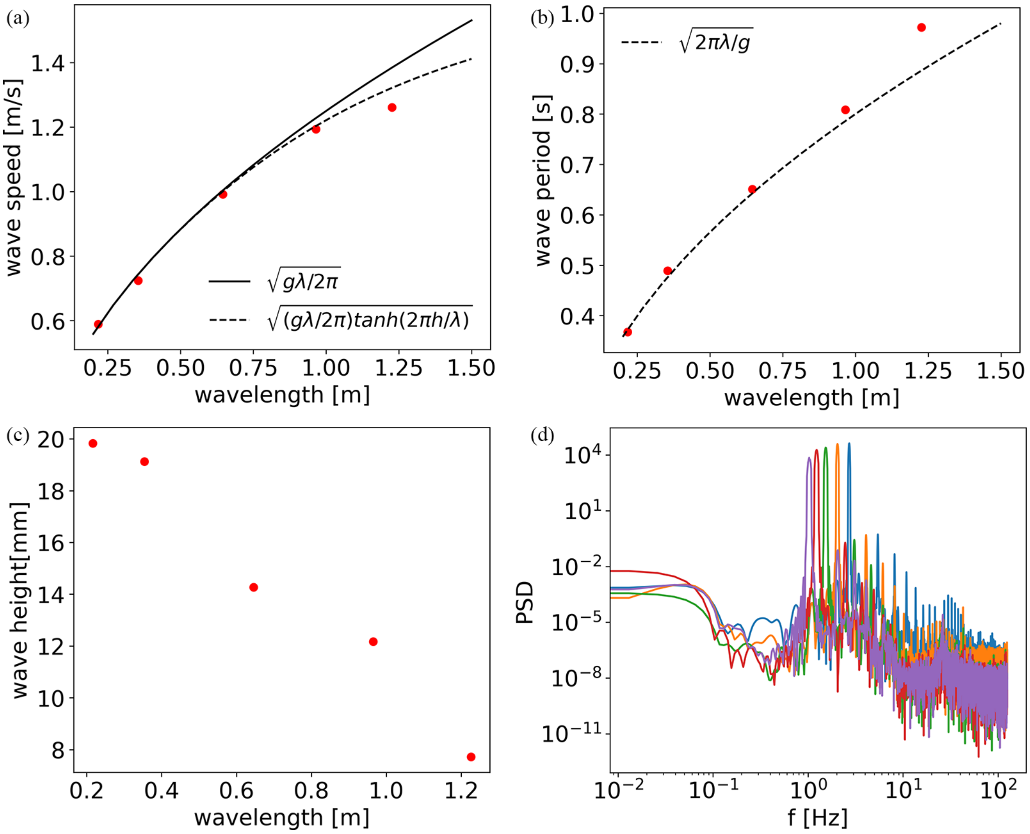

FIG. 10. Measured wave speed as a function of wave length compared to the relation according to linear wave theory for deep water waves and transitional gravity waves [92] (a), measured wave period as a function of wave length compared to the relation for deep water gravity waves [92] (b), measured wave height as a function of wavelength (c), and the power spectrum of wave height (d).

the measured wave shapes, and Fig. 10 shows in more detail the measured wave properties. Up to a wavelength of approximately 0.6m, the measured wave speed matches the equation for deep-water gravity waves [92], which is as expected given the water depth of 0.29 m. For the wave conditions with a larger wave length, the wave velocity follows more closely the equation for transitional gravity waves [92]. The wave height reduces with wave length, and varies from 0.02 to 0.008 m. Scaled to full-scale conditions, these waves correspond to a wave height of 3 to 8 m. Table V gives an overview of wave conditions that can be generated in the test setup.

Since the main objective for the experimental setup is to preserve kinematic similarity as much as possible, so that the aerodynamic effects can be studied, the ratio of wave height and wavelength to wind turbine diameter, and the ratio of wave speed to wind speed need to be considered.

The PSU wave paddle and water tank for this wind tunnel experiment can generate waves with a wavelength of 0.2 up to 1.2 m. Compared to a reference turbine with rotor diameter of 60 m, these wavelengths correspond to full-scale waves with a wavelength of 87 m up to 490 m. Deep water waves with these wave lengths, have a wave period of 7 to 17 s, which correspond to typical ocean wave conditions. However, due to not fulfilling Froude scaling, the wave period of the waves in the experiment is relatively larger, and the wave speeds relatively smaller. Full-scale deep-water waves with a wave length of 490 m have a wave speed of 28 m/s, while the wave speed in the experiment corresponds to 11 m/s in full-scale conditions. The wave speed needs to be considered when analyzing the results as it can affect the spatiotemporal correlation of motion and power

TABLE V. Measured wave conditions in the water and wind tunnel setup. Full-scale conditions are for a wind turbine with diameter $D = 60$ m and wind speed of $U_h = 25$ m/s.

	Lab-scale wave measurements				Full-scale equivalent		
Frequency [Hz]	Period [s]	Length [m]	Speed [m/s]	Height [m]	Length [m]	Speed [m/s]	Height [m]
2.7	0.37	0.22 (0.2Sx)	0.59	0.020 (0.13D)	87	5	8
2.0	0.49	0.35 (0.4Sx)	0.72	0.019 (0.13D)	142	6	8
1.5	0.65	0.65 (0.7Sx)	0.99	0.014 (0.1D)	258	9	6
1.2	0.81	0.97 (1.1Sx)	1.19	0.012 (0.08D)	386	10	5
1.0	0.97	1.23 (1.4Sx)	1.26	0.008 (0.05D)	490	11	3

output among turbines in a floating wind farm. Long-period waves can travel over long distances, and floating wind farms can be subject to such waves even though they are located elsewhere. Therefore, the ratio of wind speed over wave speed can be smaller than one as well as larger than one in offshore wind farms. The wave speeds in the wind tunnel range from 0.6 m/s to 1.26 m/s, thus limiting these tests to conditions where the wind speed is larger than the wave speed, such that the Reynolds number remains sufficiently large.

C. Wind farm layout

The wind turbine power output in an array of turbines decreases with downstream position, due to superposition of wakes. Though it can take up to tens of rows of turbines to reach a fully developed state [49,93], it is generally found that after three rows of turbines, the turbine power output stabilizes, i.e., it becomes independent of downstream distance [46,94]. Similarly, the flow statistics undergo the largest changes in the first few rows of the wind farm [72]. A wind farm with four rows and three columns of floating turbines is chosen to be scaled to the PSU wave tank, with flow measurements to be taken between the third and last row.

Considering the dimensional limitations of the wind tunnel test section, a wind turbine diameter of 0.15 m, a streamwise spacing of $Sx/D = 6$, and a spanwise spacing of $Sy/D = 3$, are selected. The streamwise spacing is slightly less than typically used in newer offshore wind farms (e.g., spacings similar to $Sx/D = 7$ or larger in some cases [94]), which is selected to maximize the number of rows in the available wind tunnel test section. A slightly smaller spacing will in effect increase the impact of wake losses on the power output of downstream turbines, which can reveal more clearly changes in wake interactions. The spanwise spacing is smaller than generally used in wind farms (e.g., spacings similar to $Sy/D = 5$–7 or larger in some cases [94]), which are designed for variable wind directions. However, transverse turbulent wake spreading is slow compared to the streamwise velocity, and in an atmospheric boundary layer turbine wakes usually exhibit linear wake spreading with a wake expansion coefficient on the order of $k \approx 0.08$, resulting in a wake growth governed by $D_w = D + 2kx/D$. Again, a relatively smaller spanwise spacing is in effect a scenario which will reveal interactions more clearly [95].

D. Wind tunnel inflow

The clean low-turbulence flow at the inlet of the wind tunnel test section is used without active or passive turbulence grid or generators. At the start of the wind tunnel test section a turbulent boundary layer will start, triggered by three plastic chains, with a height of 25 mm, located on the floor in perpendicular direction to the flow, and the step change between the wind tunnel floor and water height. For the experiments with a floating wind farm, an internal wind farm boundary layer will develop starting from the first row of turbines. Given that there is no background turbulence in the inflow, the turbulence seen by the downstream turbines is thus mainly generated by wakes of

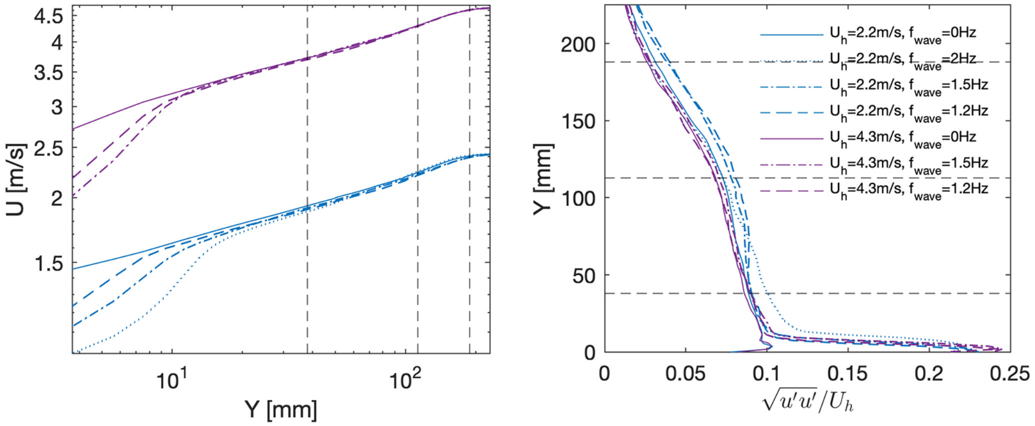

FIG. 11. The measured inflow conditions for different wave conditions used to measure the single turbine performance. The measured inflow is shown for two different wind tunnel speeds, corresponding to a free-stream velocity of 2.2 and 4.3 m/s. Black dashed lines show the top-tip, bottom-tip and hub height on the velocity profile (a) and turbulence intensity profile (b).

upstream ones. Due to the lack of a boundary layer inflow with large turbulent structures, a slower wake recovery is expected for the first row of turbines, resulting in a high power drop. But, for downstream turbines, the increased turbulence will result in an increased wake recovery, and thus power output. We recall that generally the turbine power stabilizes quickly by the second and third row [49]. The absence of a boundary layer inflow with typical very-long streamwise meandering turbulent structures will reduce the correlation in power outputs between turbines due to wind fluctuations. However, this allows us to focus on correlations that may result from dynamic wake changes due to floating wind turbine motions.

V. SCALED FLOATING WIND TURBINE TEST

The scaling methodologies applied to the scaled turbine model are explored by placing a single structure in the PSU wind tunnel and performing motion and power measurements for different wind and wave conditions, as shown in Fig. 12. For these tests, the incoming wind speed is measured using 2D-PIV of a streamwise-vertical plane, using a single 4M camera (see Appendix A). Figure 11(a) shows the measured velocity profiles for two different wind tunnel speeds, corresponding to a free-stream velocity of $U_h = 2.2$ m/s and $U_h = 4.3$ m/s, and different wave conditions. The solid colored lines show the measured velocity profile for a wind-only condition. Black dashed lines indicate the bottom-tip, top-tip, and hub-height, showing that the turbine operates mostly in the logarithmic layer of the velocity profile, up to a height just below the boundary layer height. The turbulence intensity at hub height is around 10% for both cases, as shown in Fig. 11(b).

A National Instruments NI USB 6216 acquisition card is used to measure the current of the DC generator at a sampling rate of 10 kHz. The rpm of the turbine is controlled with a 200 Ohm variable resistor. The commutator signature in the current power spectrum is used to determine the rpm of the rotor. This method was first validated using a separate optical tachometer on a fixed bottom turbine during the tests by Ferčak *et al.* [60], and was found to be in good agreement thanks to the strong commutator signature. This spectral approach is found more reliable than using an optical tachometer for a floating wind turbine, because the constant motions make alignment of the sensor with the rotor unreliable. The power coefficient is measured for two wind speeds; a hub velocity of $U_h = 2.2$ m/s and $U_h = 4.3$ m/s, corresponding to Reynolds numbers of $\mathrm{Re}_D = 2.2\times10^4$ and $\mathrm{Re}_D = 4.3\times10^4$.

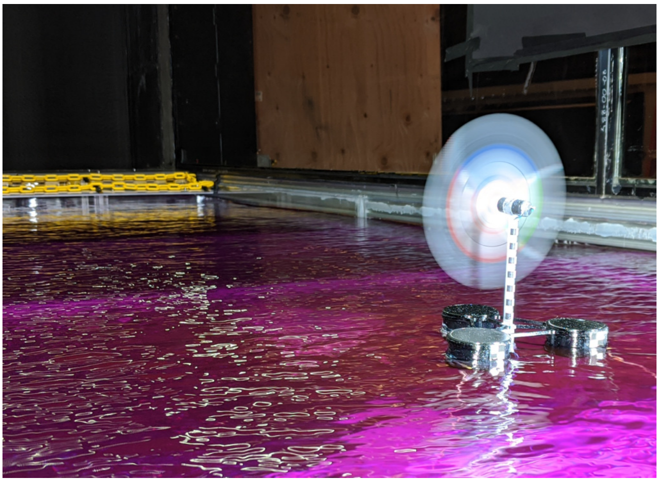

FIG. 12. Photo of a single floating wind turbine in the wind tunnel subject to 1.2 Hz waves.

The motion of the floating turbine is tracked with a stereo camera configuration, as described in Sec. III B. The measured turbine motion trajectories and corresponding power spectral density are shown in Fig. 13 for different wave conditions and for a tip speed ratio of approximately TSR $\approx$ 4.5, which is close to optimal (TSR = 4.8–5, depending on the wind speed as discussed below). In the case of no wave forcing, the motion of the floating turbine is relatively small. The pitch angle oscillates around its mean with an amplitude of $\pm 2^\circ$ for the low speed case, and $\pm 1^\circ$ for the higher speed case, indicating an effect of the mooring under higher wind loads. In comparison, tests of the DeepCWind turbine with dynamic wind loads only and for a mean hub velocity of 20 m/s (in full-scale conditions) measured a variation of $\pm 2^\circ$ around the mean pitch angle [84]. Long period sway motions are measured at frequencies on the order of 0.1 Hz (St = 0.003 to St = 0.007). For a wave frequency of 1.5 Hz, a strong pitching motion of $\pm 10^\circ$ is present, suggesting that the natural frequency for pitch is excited. A periodic yaw motion is also introduced, however, at a frequency four times smaller than the wave frequency. Yaw motions are within -10° and $+8^\circ$. For a wave frequency of 1.2 Hz, the pitching motion is reduced to $\pm 5^\circ$, but the strong yaw instability is still triggered. For comparison, Hall and Goupee [96] show pitch angles fluctuating between 0° and 8° for a full-scale turbine operating in 20 m/s dynamic wind and sea conditions. This indicates that the magnitudes of measured pitch angles are reasonable for extreme conditions. The periodic yaw motion is measured at a frequency of $1/4$th of the wave frequency. The frequency of the yaw-instability jumps to a frequency of $1/2$ of the wave frequency for higher wind speeds, as shown in Fig. 14. Under higher wind loads, the mooring makes the wind turbine response stiffer, and the ratio of yaw velocity to wave speed changes, increasing the natural frequency of this yaw instability. For the low wind speed of 2.2 m/s and the wave with a frequency of 1 Hz, the yaw instability is gone, and the pitching motion is largely reduced, a clear heave motion is still present. For larger wind speeds, the yaw stability remains triggered for the 1 Hz wave (not shown), indicating the importance of the wind and wave load balance in determining the turbine motion. In general, it is concluded that the tested wave and wind conditions, together with the scaled floating wind turbine design, generate a number of extreme conditions with well defined pitch, yaw, heave, sway, roll and surge motions. The amplitudes of all motions are in a reasonable range (i.e., maxima of pitch up to 10 degrees, sway and heave amplitudes up to 0.05D, and surge amplitudes up to 0.1D [75,97]), considering the conditions. Though some conditions result in relatively large yaw misalignment angles up to 10 degrees. The wind-only and 1 Hz wave condition result in roll angles smaller than 0.5 degrees, in agreement with results in the literature for full-scale turbines [97], though for the 1.5 and 1.2 Hz larger values up to 2 degrees are observed triggered by the large yaw motions.

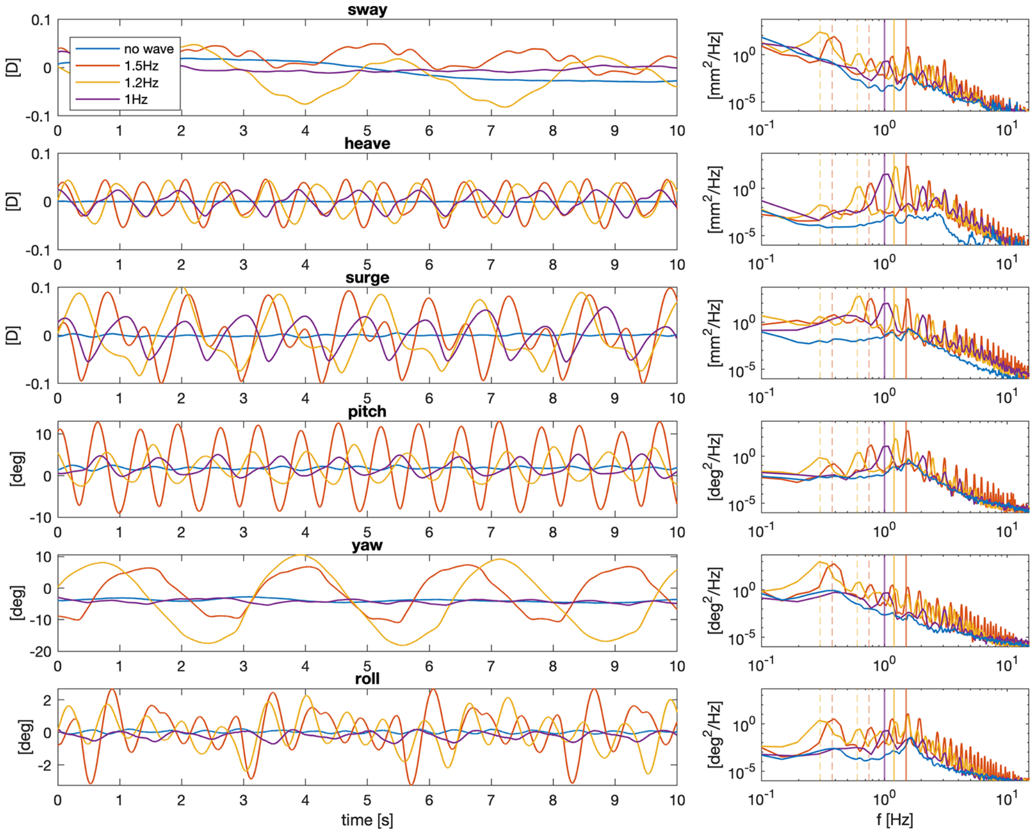

FIG. 13. Motion time trajectories of a single scaled floating wind turbine subject to a hub wind speed of 2.2 m/s. Vertical colored lines in the right panels indicate the wave frequencies, and their subharmonics.

Figure 15 shows the measured motion for three different wind speeds, with no external wave generation. The results show a sensitivity of turbine motion to the incoming wind speed. A higher wind load results in a larger mean pitch angle. The pitch of the turbine at the lowest wind speed indicates a slight forward leaning of the turbines, as the floater ballast is selected for a higher wind speed, and there is no active re-balancing. For the lowest wind speed, the motion fluctuations are generally smaller, except for pitch, which is triggered at the natural frequency of the model. For the higher wind speeds, the pitch natural frequency is not as strongly triggered, which indicates the effect of higher tension on the mooring lines. The hub velocity of 3.6 m/s triggers a strong heave, pitch, and yaw fluctuation at multiples of the heave natural frequency, not seen for the other wind speeds. The motions are thus wind load sensitive.

The power spectra of turbine motion (the right panels of Fig. 15) show distinct peaks at the wave frequencies. There are also peaks at multiples of the excitation wave frequency. Motion frequency peaks go as low as 1/4 of the wave frequency for sway, yaw, and roll. Higher-order harmonics are visible up to 10 Hz. The Strouhal number of the wave excitation ranges from 0.05 to 0.08 (if scaled with the hub height wind speed ($U_h = 2.7$ m/s) in the final wind farm experiment). But due to the higher-order harmonics, smaller amplitude motions are present up to a Strouhal number of St ≈ 0.5.

The power of the floating turbine is measured for a range of tip speed ratios, wind speeds, and wave conditions. For each condition, the electric power is measured for a duration of 30 s. Simultaneously, and synchronized, the motion of the turbine is tracked. Figure 16 shows the resulting measured power coefficients as a function of tip speed ratio. For a hub velocity of 4.3 m/s,

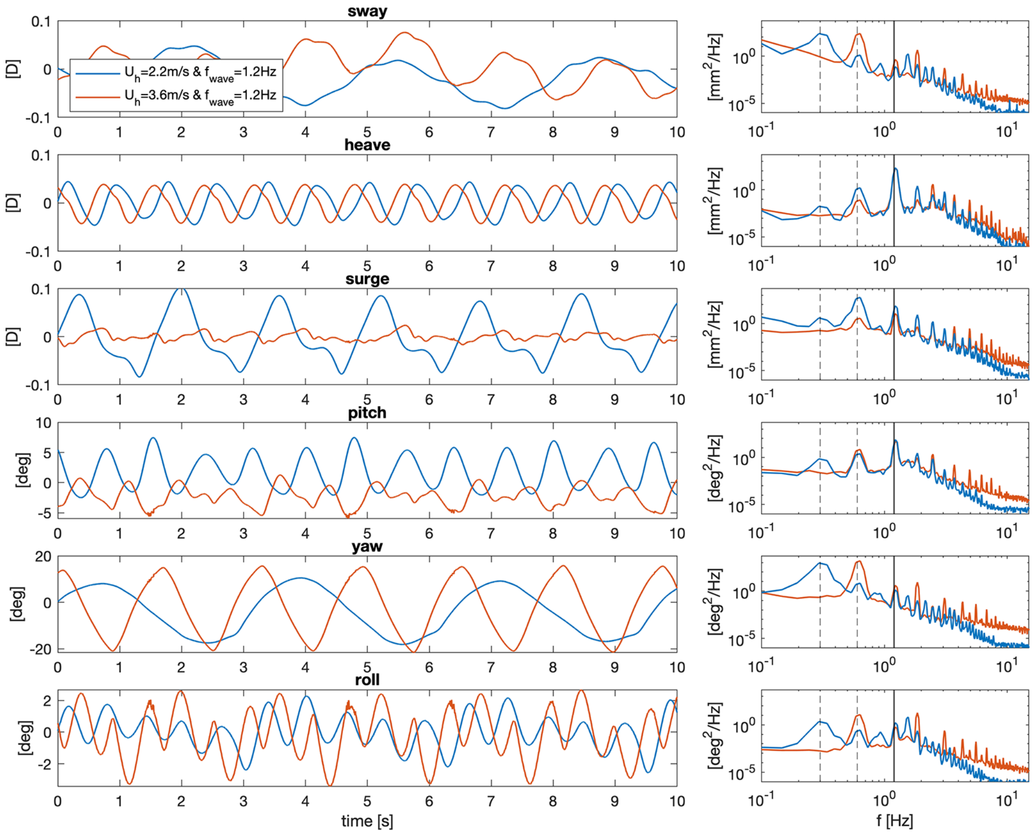

FIG. 14. Motion trajectories of a single floating wind turbine subject to a wave with frequency of 1.2 Hz, and for two wind speeds. The vertical black lines in the right panels indicate the wave frequency and its subharmonics.

the maximum power coefficient is $C_p = 0.25$, and is reached at a tip speed ratio of $\mathrm{TSR} = 5$, as shown in Fig. 16. For the lower wind speed of 2.2 m/s, the power coefficient is slightly smaller ($C_p = 0.24$) and is reached at a slightly lower tip speed ratio ($\mathrm{TSR} = 4.7$). For the purpose of these tests, the power coefficient differences are small enough to conclude that turbine operation is Reynolds number independent for the range of inflow velocities. Interestingly, though large misalignments are observed in the tracked motion, the measured power coefficient shows only a small sensitivity to the wave conditions. However, for the lower wind speed, the power coefficient shows differences between wave conditions, at the point of maximum power.

Figure 17 shows the power spectrum of the motor current signal measured for a hub wind speed of $U_h = 2.2$ m/s ($\mathrm{TSR} = 3.9$), and for a hub wind speed of $U_h = 4.3$ m/s ($\mathrm{TSR} = 4.5$). Vertical dotted lines indicate the wave periods. It is clear that for a wave frequency of 1.5 Hz, exactly at the pitch natural frequency of the model, a strong peak shows up in the spectrum due to the pitching motion. In the no-wave condition, the pitch natural frequency of the floating turbine is still excited by the wind fluctuations, yet a peak in the power spectrum is not clearly seen. For a wave frequency of 1.2 Hz, a peak becomes visible in the spectrum of the power output. This peak is much stronger for the higher wind speed case ($U_h = 4.3$ m/s), which is likely related to faster yaw-oscillation. Spectral peaks at higher frequencies ($\mathrm{St} > 0.5$) are not considered as they are expected to have an electric origin related to the DC generator, instead of being related to flow or turbine dynamics. It

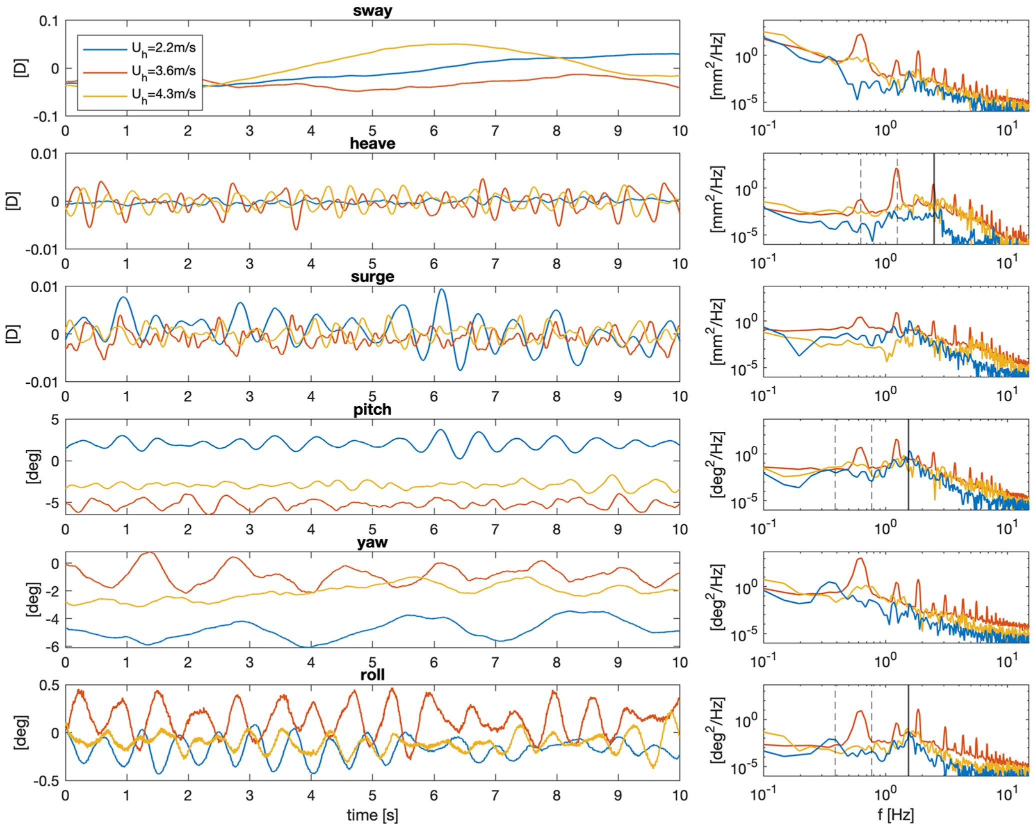

FIG. 15. Motion trajectories of a single floating wind turbine subject to no waves and for three wind speeds. The vertical black lines in the right panels indicates the natural frequency for pitch, roll or heave.

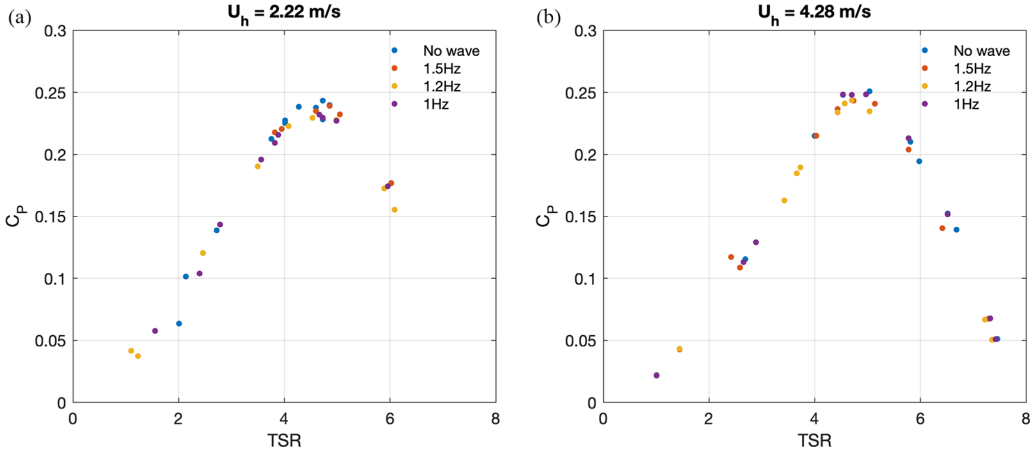

FIG. 16. The measured power coefficient for different wave paddle conditions, and for a hub wind speed of 2.2 m/s (a) and 4.3 m/s (b). The wave excitation period is indicated in the legend.

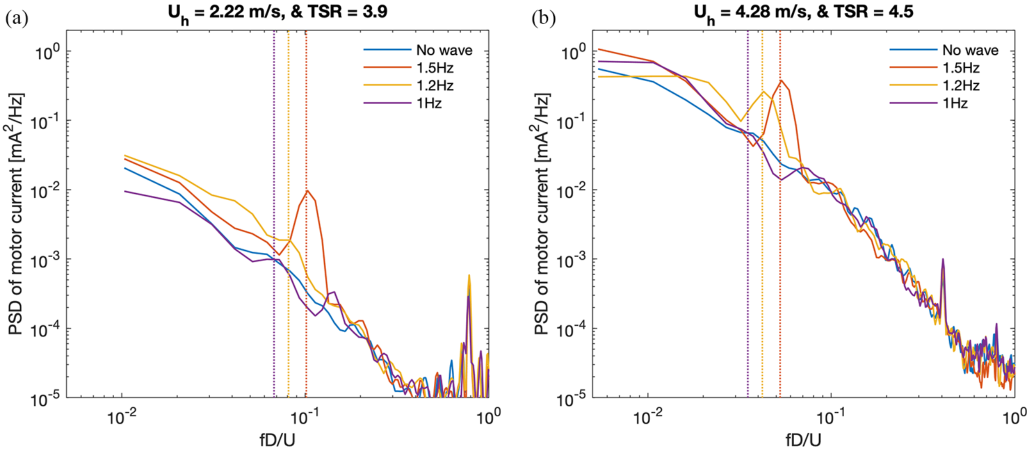

FIG. 17. Power spectral density of measured motor current for a single floating turbine subject to different wave paddle conditions, and for a hub wind speed of 2.2 m/s (a) and 4.3 m/s (b). The wave excitation period is indicated in the legend.

is concluded that even though significant dynamic misalignments are observed for the floating wind turbine subject to different wind and wave loads, the power coefficient is relatively stable.

VI. SCALED FLOATING WIND FARM EXPERIMENT

Experiments are performed for a floating wind farm consisting of 12 scaled floating turbines (4 rows and 3 columns), to study wind-wave-wake-turbine interactions for different wave conditions, see Sec. IV C for more information about the experiment and wind farm layout. The wake properties, and motion characteristics of the middle turbine in the third row are measured with S-PIV (see Appendix A), and optical tracking (Sec. III B). The optical tracking is performed separately from the PIV measurement, to provide enough light for the tracking. All experiments are performed for four different wave conditions: no external wave forcing, and a wave frequency of 1.5, 1.2, and 1 Hz. See Table V for more information about the wave conditions. A single wind tunnel speed is used for all tests discussed in this section. The electrical power of the middle turbine in each row is acquired simultaneously for each test condition. The free-stream velocity measured in a cross plane at a streamwise position of $x/D = 3$ behind the middle turbine in the third row is 4.1 m/s, calculated as the horizontally averaged velocity at the top of the PIV measurement window. The incoming hub height velocity for the middle turbine in the third row is estimated to be 2.9 m/s, based on the measured turbine power and power coefficient (as shown in Fig. 16). The TSR of the floating turbines are tuned in the no-wave condition, assuming that the turbine would operate under a classic greedy control approach so that the optimal TSR is maintained. Practically, this is implemented by optimizing the tip speed ratio of each turbine by changing the electrical resistor until maximum power is reached as calculated from the measured current (used to estimate motor torque) and rotational frequency (calculated from the commutator signature in the spectrum of the motor current). The turbines are tuned in order of row number, starting with the first row. In this section the measured motion of the turbine is first presented, followed by a discussion of the wake and power output measurements.

A. Measured motion within the scaled wind farm

For each S-PIV measurement, a separate test is done to measure the motion of the floating turbine in the middle of row 3, using the setup described in Sec. III B. During these tests, the two cameras

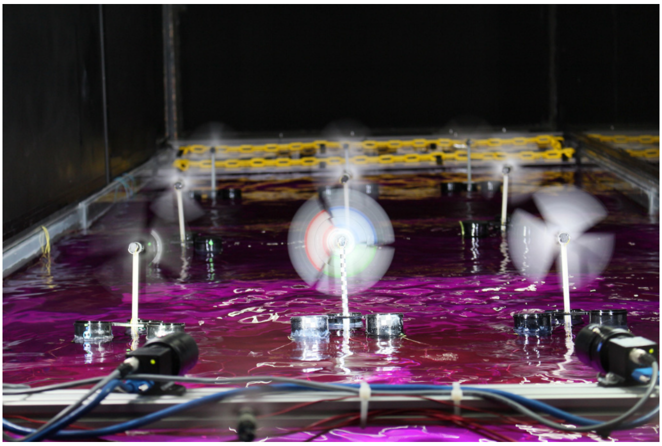

FIG. 18. Photo of the optical tracking camera setup in the wind tunnel with the floating wind farm.

for tracking are positioned inside the wind tunnel; see Fig. 18. While the fourth (and last) row of turbines are not needed for this measurement, it is noted that they operate in partial wake of the camera mount, which is positioned just above the water surface. The last row of turbines and the cameras are assumed to have no or minimal upstream effect on the motion of the turbines in the third row, as the cameras are positioned five turbine diameters downstream.

Figure 19 shows the measured motion for the six degrees of freedom, and the corresponding power spectra. There are some differences in comparison to the measurements for a single turbine in Fig. 13, which is expected to be related to a higher wind speed during the wind farm tests (a hub-height velocity of 2.9 m/s compared to 2.2 m/s) and increased wake turbulence inside the wind farm.

Similar to the previous conclusion for a single scaled floating turbine, the yaw instability frequency in waves of 1.2 Hz is higher when subject to a higher wind speed (e.g., it is found to be around $1/2\, f_{\text{wave}}$ instead of $1/4\, f_{\text{wave}}$). The higher wind speed directly impacts the sway and roll motion as well. The 1.5 Hz waves do not trigger the yaw instability, but it is present for the wave condition of 1 Hz. The amount of yaw misalignment when the yaw instability is triggered depends on the mooring. The measurements show a higher amplitude in yaw misalignment for the wind farm measurements, which is likely due to a slightly looser mooring. It is also important to note that the mean yaw angle is around 5 degrees for all wave conditions. It is hypothesized that this is triggered by partial wake overlap, which results in asymmetric inflow conditions, resulting in a nonuniform wind loading pushing the floating turbine towards a slightly yawed position.

It is concluded that each wave condition results in different and strongly pronounced turbine motions. For example, the no wave condition results in a pitch fluctuation of around $\pm 2^\circ$ at the natural frequency of the turbine, but also longer period sway variations. The 1.5 Hz wave condition results in very strong pitch oscillations, which send the wake up and down periodically, and is coupled to relatively high waves traveling through the wind farm. The 1.2 Hz wave condition, however, leads to a scenario in which the yaw instability is the most pronounced motion of the turbine, deflecting the wake left and right periodically, although there are still significant synchronized pitch motions. The 1 Hz wave condition simulates very long-period ocean waves, triggering the yaw instability at a lower frequency without significant pitch motions.

B. PIV wake measurements

In this section S-PIV measurements of the wake of the middle turbine in the third row are presented. The measurements are performed at a downstream distance of $x/D = 3$ from the third-

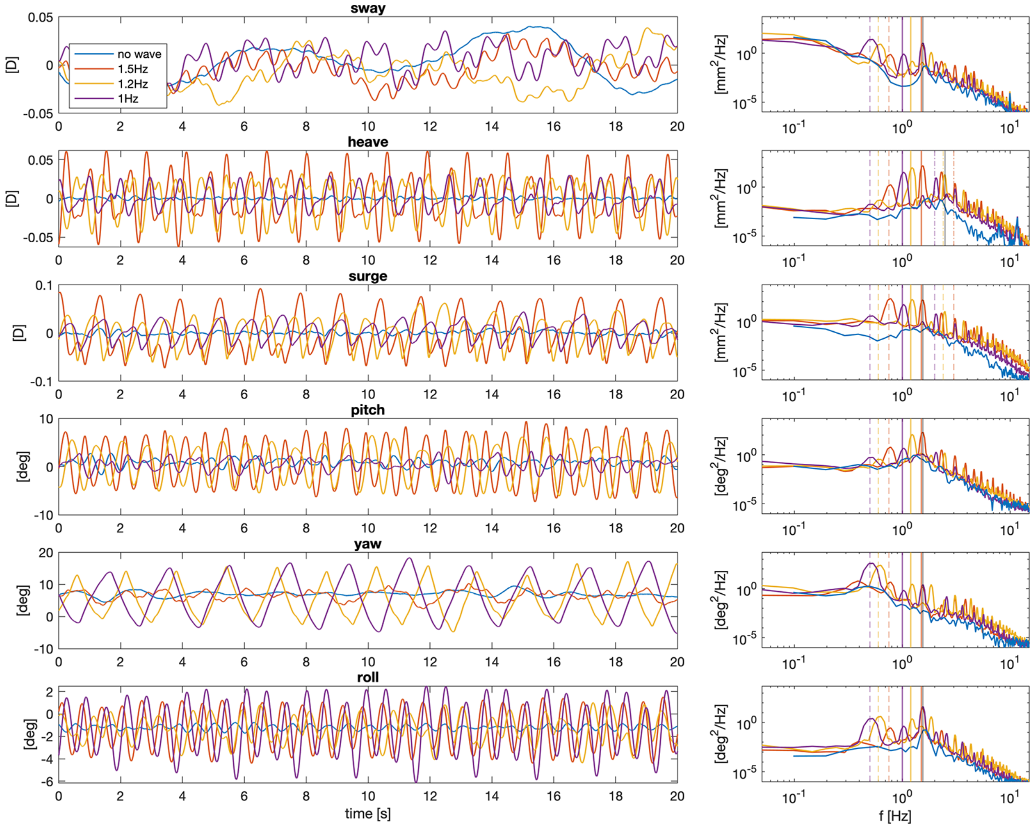

FIG. 19. Measured motion of the floating wind turbine model in the third row of the wind farm, for all four wave conditions.

row turbine. Five thousand snapshots are acquired for each condition and are averaged to calculate distributions of mean wind velocity and turbulence intensity based on the streamwise velocity fluctuation variance. The mean velocity contours are shown in Fig. 20, indicating subtle differences in wake recovery (velocity deficit), shape, and the location of maximum velocity deficit. The wakes for the 1.5 and 1.2 Hz wave conditions show the highest mean velocities and lowest wake velocities defects near the wake center.

To quantify the subtle velocity differences in terms relevant for power generation, we place a hypothetical wind turbine at various locations. The change in available power in the wake is estimated by spatially averaging U^3 over different hypothetical downstream rotor areas. Specifically, the effect of the spanwise position $\Delta z/D$ of a hypothetical wind turbine placed at the $x/D = 3$ downstream plane is studied, and its performance is compared to the aligned case with $\Delta z/D = 0$. The available power found for different wave conditions and spanwise shifts is normalized by the available power for the condition with no external waves and no spanwise shift (Fig. 21). For the condition with no external waves a spanwise shift of 0.2D (i.e., going from full to partial wake overlap) can lead to an increase in power of almost 15%. For the 1.5 and 1.2 Hz wave conditions, the available power increases by 10% even for the case with no spanwise shift, clearly showing an impact of turbine motions and wave interactions on wake recovery in a wind farm boundary layer. These values are overestimates of the actual expected differences since an $x/D = 3$ downstream distance is lower than spacings in typical wind farms, but the trends are instructive nonetheless.

In Fig. 20, the contours of streamwise turbulence intensity $\sqrt{u'u'}/U_0$ show distinct differences between wave conditions. Zones of high turbulence intensity highlight where there is high production

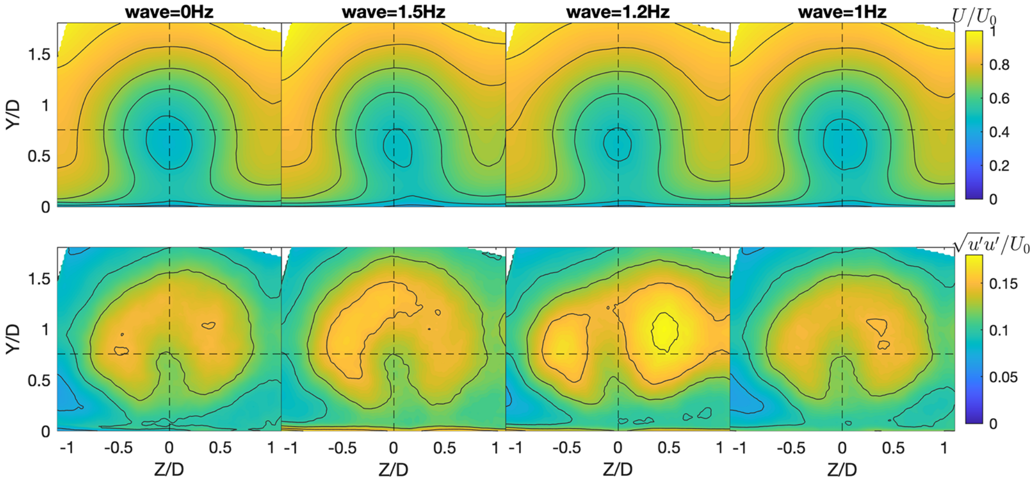

FIG. 20. Mean contours of wake velocity (top) and turbulence intensity (bottom) for all four wave conditions.

of turbulence in the top and side shear layers of the wake, but also zones where wake meandering triggered by turbine motions results in velocity variations over longer time periods. The turbulence intensity contour for a wave of 1.5 Hz shows stronger turbulence levels at the top of the wake, possibly resulting from the periodic up and down deflection of the wake. The strongest difference is seen for the 1.2 Hz wave condition. In this case, the wake width has increased, as indicated by the two pronounced zones of high turbulence intensity on the left and right sides of the wake. This pattern is consistent with a periodic horizontal deflection of the wake caused by the yaw instability. Though the yaw instability is also recorded for the 1 Hz wave condition, the turbulence intensity contours don't show the same shape. A difference between the 1 and 1.2 Hz scenario is that the yaw motion for the case of 1 Hz waves happens at a slower frequency and the pitching motion is significantly reduced. The significant difference in the wake properties between the 1.2 and 1 Hz waves highlight a potential sensitivity to the Strouhal number of rotor motions, as discussed by Messmer *et al.* [25].

To better understand the periodic wake behavior, the PIV results are conditionally averaged with the wave phase at the time of each PIV snapshot. This is practically done by considering the fixed

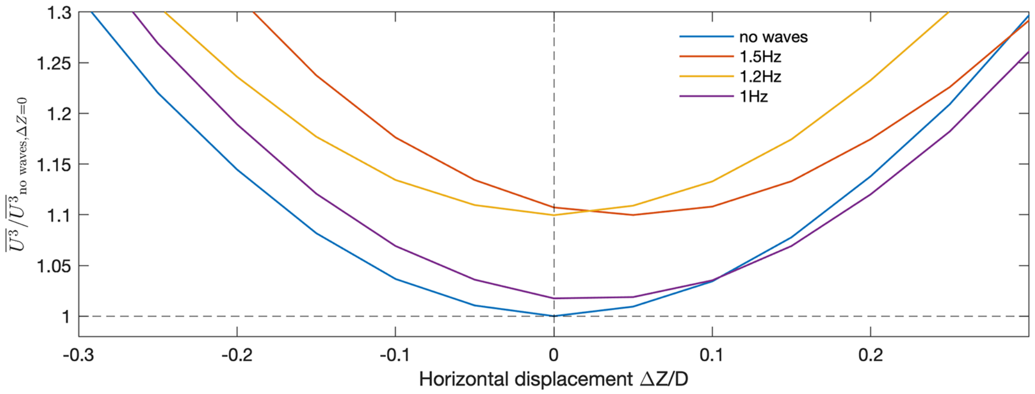

FIG. 21. Relative wake power potential as calculated by the average of U^3 over a rotor area with spanwise position ΔZ compared to the upstream turbine.

frequency of the laser pulses (i.e., 3.75 Hz), and fixed wave frequency of the wave-paddle. Based on the acquisition time of each PIV snapshot and the wave period, all snapshots are projected on to a single or double wave period, depending on the motion of the turbine that is considered. Projecting the PIV measured wave heights is very sensitive to the exact wave frequency. An optimization was performed to refine the wave frequency for optimal synchronization with the PIV results. The refined wave frequencies show small deviations from the controlled wave frequency (e.g., 1.54 Hz instead of 1.5 Hz), which can be explained by inaccuracies in the clock frequency of the Arduino used to control the wave-paddle, compared to the highly accurate timing module for the PIV measurements. Figure 22 shows the reconstructed wave shapes by projecting the mean water height in each PIV snapshot. The synchronization frequencies are indicated for each wave condition. In general very good agreement is found with the measured wave shapes captured using time-resolved LIF, as shown in Fig. 9, though now there is more variation in wave height due to a small wave-to-wave variation, and small wind effects on the water surface. The wave period is then divided in eight phase-bins, and for each phase the PIV snapshots are ensemble averaged, resulting in a conditional average of the wake contour for that specific wave phase. The number of PIV snapshots in each phase-bin is about 625.

Figure 22(a) shows the conditionally averaged mean velocity contours for a 1.5 Hz wave condition, triggering strong pitching motions. Wave phases are labeled 1–8 from bottom to top of the figures. Consistent with the discussion above, the contour plots indicate an up-and-down motion of the wake center at the frequency of the wave. For example, during phases 4 and 5, a moment of high wave height occurs at the same time and place as where the wake is deflected downwards, which can be seen from the location of maximum velocity deficit (indicated by a red dot) reaching a minimum height in comparison to the other phases. Due to the difference in wave and wind speed, the interaction between the periodically downwards deflected wake and the traveling waves will vary spatially and temporally. Figure 22(b) shows the conditionally averaged mean velocity contours for the 1.2 Hz wave conditions, triggering a strong horizontal oscillation at half the wave frequency (i.e., the wake moves left and right once within the two-wave-period window), accompanied by a smaller vertical oscillation at the wave frequency (i.e., the wake center moves up and down for every wave period). The motion measurements also showed that for this wave condition the turbine moves with a yaw oscillation at half the wave frequency, and a pitch oscillation at the wave frequency. Therefore, it is clear that the conditionally averaged wake contours show wake deflection from turbine misalignment which is synchronized with (and triggered by) the waves. Consequently, these wave conditions show a strong left and right deflection of the wake center at different wave phases at the location of the PIV measurement plane. Since the yaw and pitch oscillations happen at multiples of the wave frequency, they are synchronized with one another. The moment of maximum upwards wake deflection happens at a moment of minimal yaw misalignment (i.e., phases 4 and 8). The moments of maximum yaw deflection are seen for phases 2 and 6, corresponding to a phase in which the wave almost reaches its maximum wave height. Figure 22(c) shows the conditionally averaged mean velocity contours for the 1 Hz wave, which also results in a strong yaw oscillation, but with weaker pitching motion. It is noticed that the yaw deflection is smaller, explaining why the mean turbulence intensity contour in Fig. 20 is more similar to that of the no wave condition.

C. Floating wind farm power output

In this section the spectral features of the power output of each individual turbine, and of the aggregated power are investigated. Figure 23 shows the power spectral density of the measured power for each row. The power signals are normalized by their mean value: $P_{\mathrm{row},i}/\overline{P}_{\mathrm{row},i}$ before calculating the power spectral density. The power characteristics of the first row differ from the other three rows, due to the different inflow conditions: a higher inflow velocity with minimal turbulence levels. The other (downstream) rows operate in waked conditions, for which the velocity is reduced, and turbulence has increased. Knowing the power coefficient from the single turbine calibration, the incoming hub height velocity can be estimated. The reconstructed hub height wind speeds

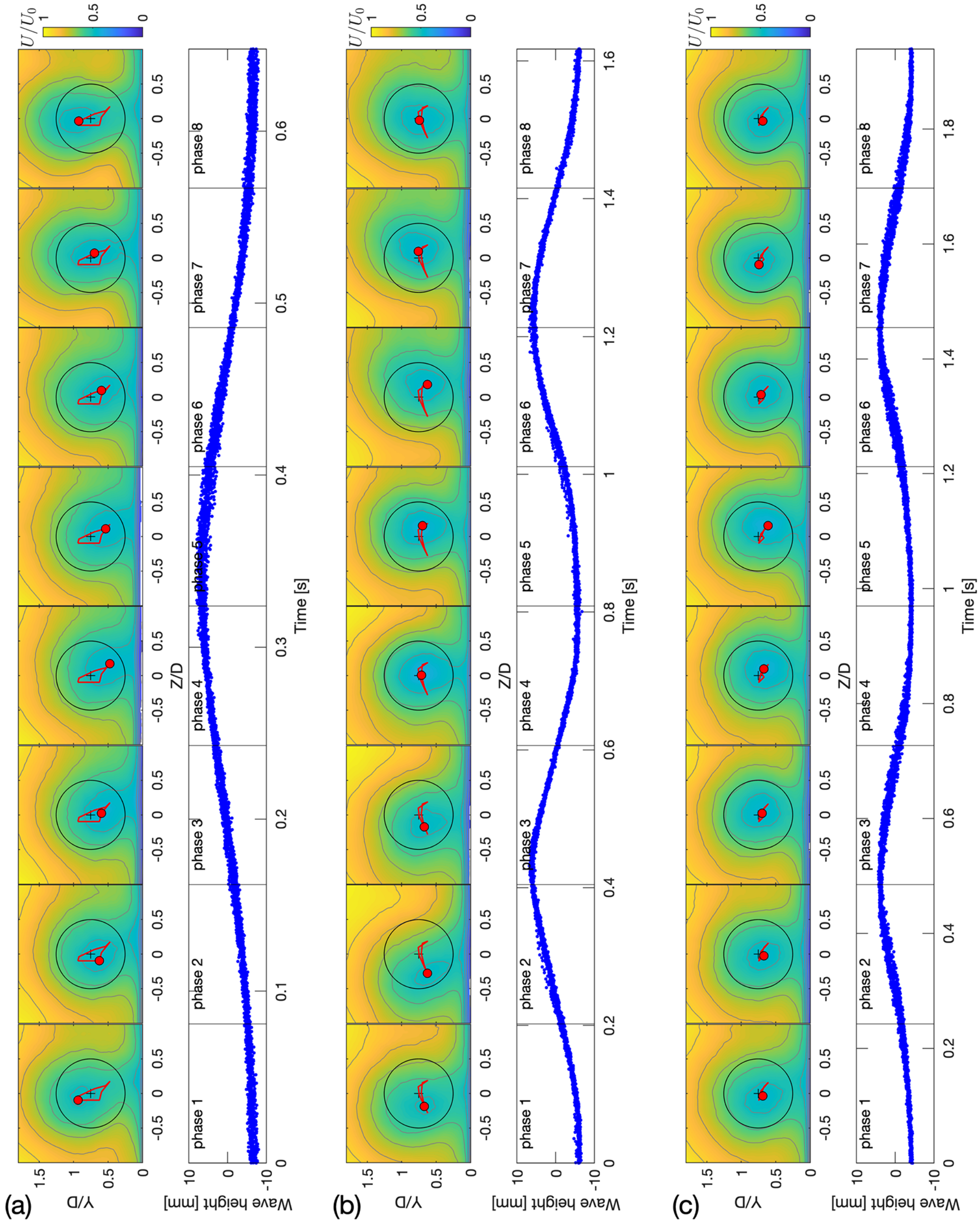

FIG. 22. Conditional averages of wake phases for 1.5 Hz (a), 1.2 Hz (b), and 1 Hz (c) waves, accompanied with a plot of wave height reconstructed from all PIV snapshots, projected onto a single (a) or double (b), (c) wave period using a synchronization frequency of 1.5437 Hz (a), 1.23647 Hz (b), and 1.03116 Hz (c). The maximum velocity deficit is indicated with a red dot, and its trajectory by a red contour line. The reference rotor position is indicated by a black circle to indicate wake changes.

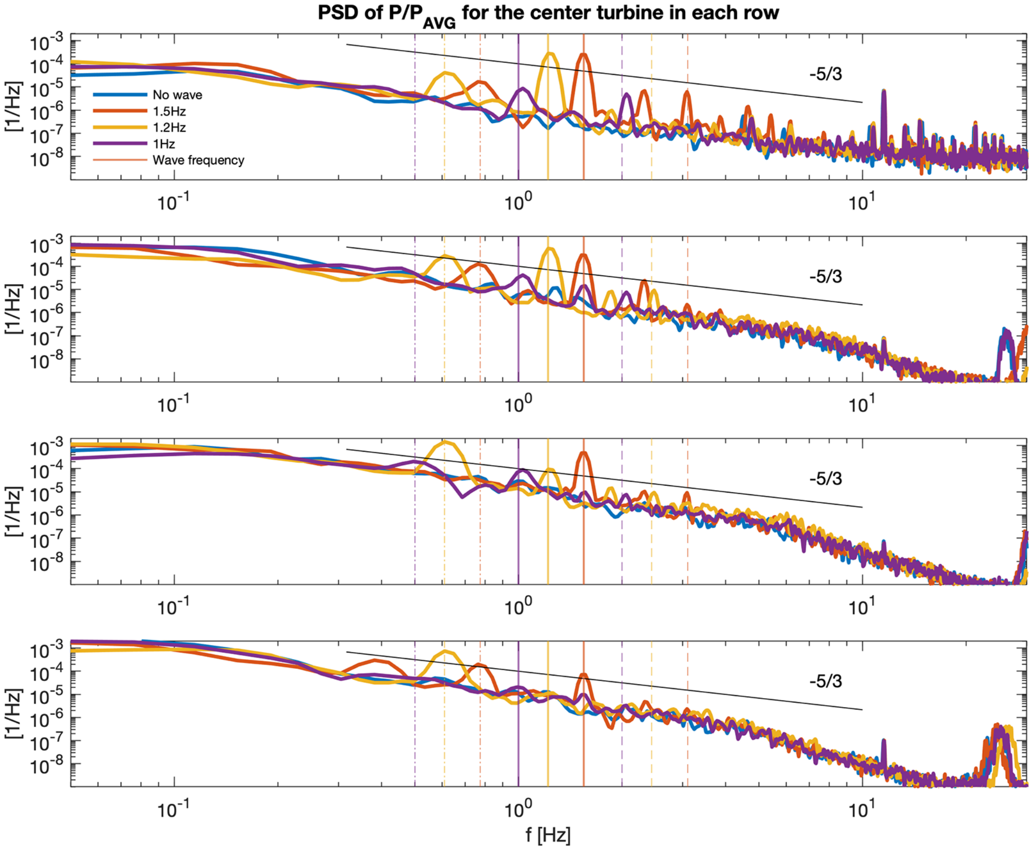

FIG. 23. Power spectrum of turbine power normalized by its time-average ($P_i/\overline{P_i}$) for the middle turbine in rows 1–4, from top to bottom. Vertical lines indicate the wave frequencies (–), their second harmonic (– –), and subharmonic (–.).

for no wave conditions are estimated to be 3.9 m/s for the first row, 2.6 m/s for the second row, 2.9 m/s for the third row, and 2.5 m/s for the last row. The spectrum of the power output is a result of the incoming wind fluctuations and the wave oscillations. Given that for the first row, turbulence levels are low, the spectrum is mostly determined by wave oscillations. The spectra show a clear peak at the 1.5 and 1.2 Hz wave frequency. For the 1 Hz waves, the peak is less pronounced, which is expected due to the more subtle motions of the turbines in these conditions. The 1.2 Hz wave conditions show a spectral peak at half the wave frequency due to the periodic yaw motion. For the 1.5 Hz wave condition, a peak at half the wave frequency appears in the spectrum for the first, second, and last row turbines. It is not clear if this motion is a result of wind speed dependence or small changes in the mooring tension. Because the motion of turbines in the other rows was not measured, this observation cannot be confirmed. For all rows, the 1.5 and 1 Hz wave conditions result in a distinct spectral peak of the power at the first harmonic, corresponding to double the wave frequency. For the 1.5 Hz wave condition, a spectral peak at the natural frequency for heave (2.5 Hz) is noticed in the power spectrum of rows 1 and 2. The spectral peak at the wave frequency for the 1.5 Hz waves is present in the power output of every row, confirming the high sensitivity of turbine power to pitching motions. The spectral peak at the wave frequency for a 1.2 Hz wave becomes smaller with increasing row number.

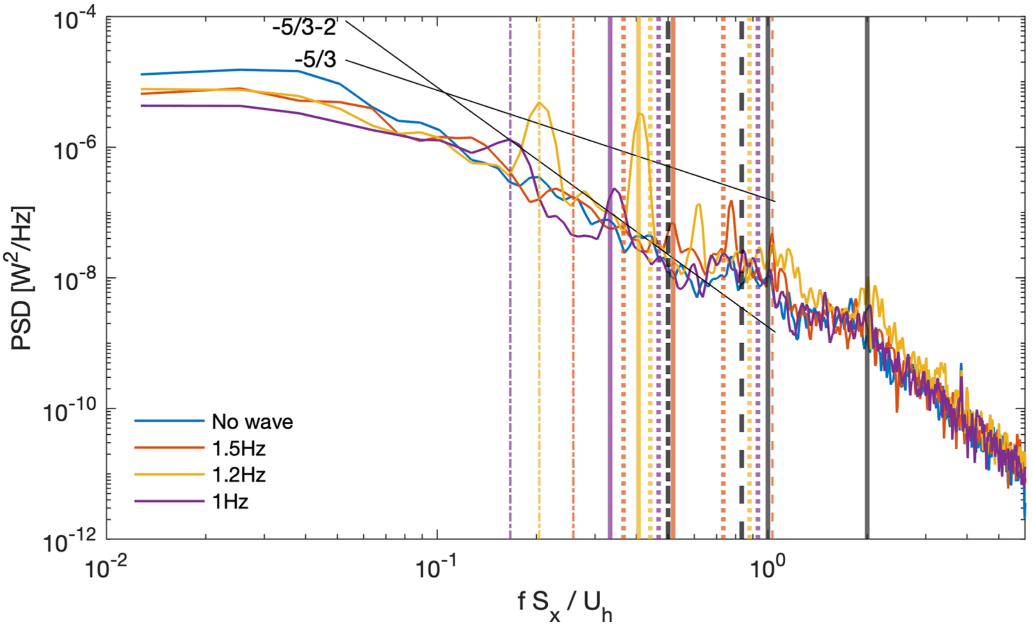

FIG. 24. Power spectrum of aggregate power of the three middle turbines in rows 2, 3, and 4. Black lines indicate: the flow-convective frequency corresponding to one and two turbine spacings S_x (–), the natural frequency for heave (– –), and the natural frequency for pitch (–.). Colored lines indicate the wave excitation frequencies (–), half of the wave frequency (–.), double the wave frequency (– –), and the frequency and first harmonic related to wave speed and turbine spacing v/S_x (:). A power-law scaling of -5/3-2 is shown to indicate the spatiotemporal sampling effect established for fixed bottom wind farm arrays [100].

Figure 24 shows the power spectrum of the combined wind farm power of the center turbine in rows 2, 3, and 4. The turbine in row 1 is left out of this aggregate because it is subject to different inflow conditions with a higher wind speed and minimal turbulence levels, and here we aim to study specifically turbulent wind farm conditions. Including row 1 does not drastically change the behavior, though it may obscure possible spatiotemporal correlations due to coherent turbulent structures. The power spectrum of the combined power shows distinct peaks at different frequencies, which can be related directly to wave frequencies, but also to spatiotemporal correlations in power fluctuations of turbines, due to the advection of turbulence and wave displacement. The wind advection time between two rows of turbines S_x/U_h, with the advection velocity estimated by the hub velocity, results in a phase lag between a turbine motion (and resulting power fluctuation) in one row, and the instance that a downwind turbine is exposed to a changed wake conditions (with resulting power fluctuation). The phase lag affects how much the power fluctuations are correlated, or anticorrelated. Similarly, the wave travel time between two rows of turbines S_x/v will result in a phase lag, which determines how the power fluctuations caused by turbine motion in one row will correlate or not with a downstream row. For the 1.5 Hz wave condition, there is no peak visible at the frequency related to the wave speed and turbine spacing v/S_x in the combined power spectrum, and the peak at the wave frequency is also strongly reduced. It is expected that this is the result of the wave phase lag partly anticorrelating the pitch motions. For example, the correlation coefficient ρ of two sine functions with a frequency of 1.5 Hz and phase shift of the wave travel time $S_x/v \approx 0.9$ s, is $\rho \approx -0.6$, thus anticorrelating partly the pitching motion of two consecutive turbine rows. Similarly, the phase shift of the wind-advection time is $S_x/U_h \approx 0.3$ s, resulting in a correlation coefficient of $\rho \approx -1$. However, the effect of the wind-advection on the correlation of power fluctuations from turbine motions is less straightforward, because it relates a power fluctuation to a change in wind condition for the downstream turbine (for example a deflected wake due to a yawed rotor movement), while the downstream turbine is also making a motion which is triggered by the waves and phase-lagged with the wave travel time. The combined power spectrum for a 1.2 Hz wave still shows a distinct peak at the wave frequency, though the wave travel time results in partly anticorrelating. It is expected that this is because for this wave condition, only the power signal of the turbine in row 2 shows this peak distinctly. Thus, not leading to significant canceling out between multiple rows.

At the frequency corresponding to the flow convection time between two rows U_h/S_x, and the double of this frequency, all tested conditions (including the wind-only measurements) show a broad, but less pronounced peak in the spectrum. This shows that even though the aggregate is taken over a small number of turbines, and rows (i.e., three), a spatiotemporal correlation in output power due to convection of turbulent structures results in a peak of the power output. Similar observations were made for a fixed-bottom scaled wind farm with twenty rows, subject to a turbulent boundary layer with long streamwise-meandering turbulent structures [49]. The spatiotemporal sampling of the inflow by a wind farm was described analytically, showing that for wind farms with more than three rows distinct peaks can appear in the power spectrum if the inflow has large turbulent structures that remain correlated over long distances as they travel through the wind farm [98,99]. In the present experiment, there is no space in the wind tunnel test section to develop a boundary layer with such long meandering structures. Given that we see these correlations in the aggregate power over only three turbines, it is hypothesized that the motion of the turbines become synchronized between different streamwise aligned turbines, due to wake interactions. This can be the result of a turbine in row 2 making a sway motion, deflecting the wake, such that a downstream turbine in the next row at a time S_x/U_h later notices a change in inflow conditions, and moves in response. The broad peak at $fS_x/Uh = 1$ is also close to double the wave frequencies, though no distinct peaks arise, except for the 1.5 Hz wave condition, for which the wave length is very close to the turbine spacing. For the 1.5 and 1.2 Hz waves there are two other distinct peaks in the range of $fS_x/U_h = 0.6$–0.8, which are also seen in the individual spectrum of the turbine in row 2.

In Fig. 25, the measured cross-correlation of power signals between two turbines in the middle of a row is shown as a function of time-delay between the signals. For the no-wave condition, it is noticed that the auto correlation of the power signal stays correlated over a very long time. This trend is especially noticeable when compared to results for fixed bottom turbines subject to a turbulent boundary layer [95], which show distinct peaks at the turbine spacing convective timescale, but quickly become decorrelated over a time of $tU_h/Sx > 3$. This indicates slow variations in power output, which may be a result of the slow sway motions of the upstream turbine. Similarly, the cross-correlations with downstream turbines remain correlated over a long time. A maximum cross-correlation is reached at a convective flow-time corresponding to increments in turbine spacing, highlighting how slow turbine motions can correlate the power outputs of downstream turbines via convected wakes. These findings are in agreement with Fu *et al.* [39] who found an increased auto correlation of the power signal for oscillating rotors. For the no-wave conditions, the maximum cross-correlation in power output between rows 2 and 3 is around 0.55, which is similar in magnitude as seen for fixed bottom turbine by Bossuyt *et al.* [95]. However, in this case the high correlation is expected to be related to the effect of wake variations from slow turbine motions (e.g., sway), instead of large turbulent structures, given that these are not present in the inflow in this experiment. For the 1.5 and 1.2 Hz wave conditions, the auto-correlation of the power in row 2 shows a strong oscillation at the wave frequency due to the periodic turbine motion. For the 1 Hz wave, the oscillatory behavior has disappeared, highlighting the slower and likely more variable motion over time. Interestingly, the cross-correlations with downstream turbines are reduced in magnitude for these long-period waves (<0.25). As discussed above, because of the phase-lag between motions in different rows, and due to the wave velocity, the correlation from turbine motion is reduced for the conditions studied here. For the no-wave condition, this is not the case, because the turbine motions are wind-driven as wakes travel downstream affecting other turbines, synchronizing the motion frequency with the convective flow frequency. For a wave condition of 1.5 Hz, the instantaneous power of a turbine in

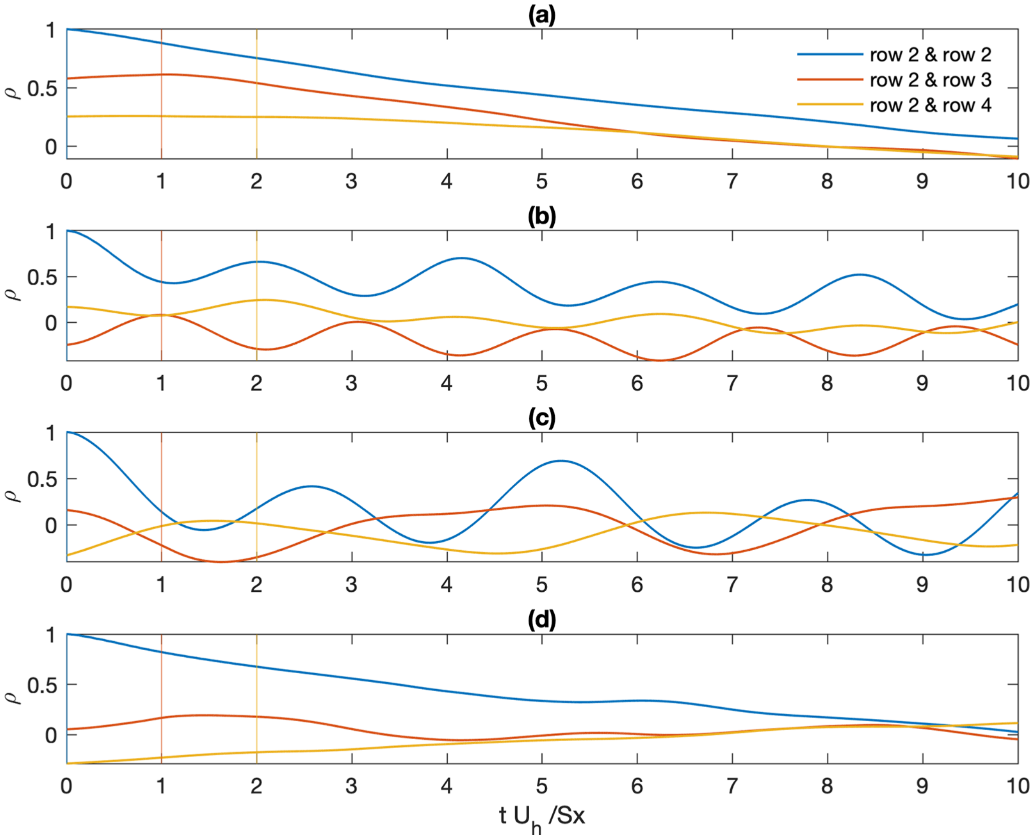

FIG. 25. Cross-correlation of turbine power signals for wind-only (a), 1.5 Hz wave (b), 1.2 Hz wave (c), and 1 Hz wave (d) conditions. Vertical lines at $tU_h/S_x = 1$ and 2 indicate the convective flow time between rows 2 and 3, and between rows 2 and 4.

rows 2 and 3 show a slight anticorrelation. This is a result of the wave having a wavelength equal to $0.7S_x$, anticorrelating the motion of the turbines slightly. For a wave of 1.2 Hz, the wavelength measures $1.1S_x$, and is thus close to the turbine spacing, which explains the instantaneous correlation between rows 2 and 3, and anticorrelation between rows 2 and 4. Anticorrelations in turbine motion and resulting power output can result in reduced power fluctuations in the combined power output at certain frequencies. For example, in Fig. 24, the power spectrum of the 1 Hz wave conditions is smaller than that of the no-wave condition in the 0.5–1 Hz range, indicating an anticorrelation of turbine motions.

Figure 26 shows the mean power of the middle turbine in each row, normalized by the power of the middle turbine in the first row, for the wind-only condition ($P_i/P_{1,\text{no waves}}$). It can be seen that for the 1.5 and 1.2 Hz wave condition the power in the first row reduced due to the increased misalignment. However, in the second row, the power increases more. This shows that the motion of the turbines studied in this paper can enhance wake recovery, especially in situations where the wake recovery is slow (e.g., the wake of the first row of turbines is subject to less background turbulence resulting in a smaller wake recovery rate). For the power of the turbine in the third row, the effect less pronounced. Compared to the wind only condition, the total farm power increases with 0.7% when subject to 1.5 Hz waves, 5% for 1.2 Hz waves, and 2.1% for 1 Hz waves.

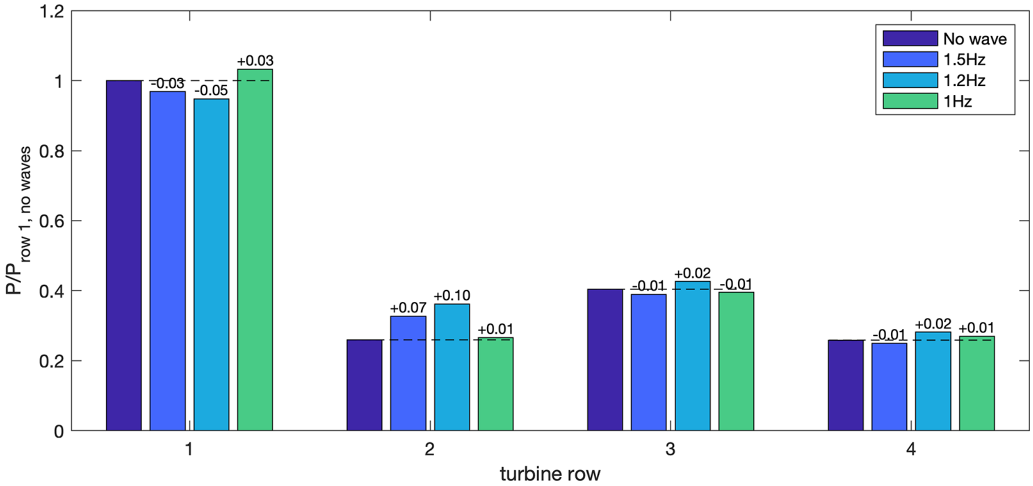

FIG. 26. Effect of wave conditions on power output of the middle turbine in each row. All measured power values are normalized by the power in the first row for the wind only condition. The normalized absolute power increase of each turbine compared to the wind-only condition is indicated above each bar.

VII. CONCLUSIONS

A floating wind farm experiment is scaled for measurements in the Portland State University wind tunnel. A design approach that deviates from geometric similarity is introduced to enable scaled floating turbine models with a realistic dynamic response even though Froude scaling is unachievable at the desired scale ratio (1:400). The method is analogous to the use of different low Reynolds number airfoil blade profiles and proportionally much larger chord lengths for wind tunnel tests of scaled turbine rotors to reproduce realistic dimensionless parameters for wake development (e.g., TSR, C_T, and C_P). Four scaling ratios comparing the relative importance of wind and wave loads to the turbine inertia are studied. These ratios highlight how the floater design can be adjusted to match the desired dimensionless natural frequency for pitch and heave motions. Using this approach, a scaled model floating turbine is designed, matching the dimensionless ratios of the target turbine with a rotor diameter of 60 m, and based on the OC5 DeepCWind floating platform. Based on measurements of the free-decay response of tilt, and heave, it is confirmed that the scaled natural frequencies are within the typical range for full-scale floating turbines. The four dimensionless ratios provide insights into how the floating model platform can be further adjusted and designed to scale to even larger rotor sizes.

The power and six-degrees of motion of a single turbine are characterized in a wind tunnel test with different wind and wave conditions. Depending on the wave frequency, distinctly different turbine motions are measured. Based on the wind-only test, it is concluded that the platform pitch motion amplitude is within typical values for full-scale turbines (e.g., sway, heave an surge motions on the order of or smaller than 0.05D, roll and yaw fluctuations smaller than $\pm 0.5^\circ$, and pitch fluctuations of $\pm 2^\circ$ for wind-only conditions). The spectra of the measured pitch motion trajectories show a strong signature of the wave frequency and its harmonics and subharmonics (e.g., double and half the wave frequency), depending on the motion and flow conditions. The Strouhal number of the wave frequency ranges around $\mathrm{St} = 0.05$ to $\mathrm{St} = 0.08$, but motions with smaller amplitudes at higher harmonics up to $\mathrm{St} = 0.5$ are also triggered. The measured power coefficient for a wind speed of $U_h = 2.2$ m/s and $U_h = 4.3$ m/s shows only little Reynolds number sensitivity for the wind speed range of interest (i.e., a variation in power coefficient of $C_p = 0.24$ to $C_p = 0.25$). The power spectral density of the turbine power output shows a distinct peak at the wave frequency mostly for the 1.5 Hz wave condition, which triggers a strong pitching motion. For the 1.2 Hz wave condition a smaller peak at the wave frequency is seen, corresponding to a smaller pitch motion at this frequency.

Wind tunnel measurements are then performed for a scaled wind farm with twelve floating turbines (4 rows and 3 columns), for high wind conditions (corresponding to $U_h = 25$ m/s in full-scale) and for three conditions with long period ocean swell waves, and one wind-only case. The power of the middle turbine in each row is measured, as well as the motion and wake of the middle turbine in row 3, for the four different wave conditions. The turbine motions show slowly varying sway variations for all wave conditions. Tests are performed for wave frequencies close to, and below, the natural frequency of the floating turbine model, resulting in very distinct motion patterns. PIV measurements show clear differences in wake recovery due to the periodic motions of the rotors. The 1.2 Hz wave condition triggeres strong synchronized yaw and pitch motion, and results in increased wake recovery, but also higher turbulence in the wake, which may affect unsteady loading of a downstream rotor. By conditionally averaging the wake measurements with respect to wave-phase at the measurement plane, a clear synchronization between wave induced rotor misalignment and wake deflection is confirmed for all three conditions with long period ocean wave conditions. The power spectral density of scaled floating turbines in rows 1 to 4 shows distinct peaks due to the induced rotor motions. Changes in the spectrum between different rows indicate differences in motion due to different mean wind conditions, and differences in velocity fluctuations due to the superposition of turbine wakes. The spectrum of the aggregate power of rows 2, 3, and 4 shows a distinct peak at the wave frequency and half the wave frequency for the 1.2 Hz wave condition, which is characterized by strong yaw and pitch motions. For the 1.5 Hz wave condition, the peak at the wave frequency is still present but strongly reduced, which could be a result of the phase shift between the pitching motion of different rows, resulting from the wave phase velocity (e.g., v/S_x is equal to 0.6 times the wave frequency of 1.5 Hz, which is close to an anti correlation). It is expected that for the 1.2 Hz wave condition the peak at the wave frequency is not canceled out, because the power fluctuation at this frequency was mostly present for the turbine in the second row, and less so for the others, thus not resulting in a canceling out of power fluctuations over multiple rows. The cross-correlation of power outputs confirms a lower maximum cross-correlation of power signals when the turbines are subject to the tested long period waves, as compared to the wind-only scenario. Compared to the correlations in power output of fixed bottom turbines, which is mostly governed by turbulent spectra of the inflow [100], the power signals can remain correlated over much longer times in the absence of long-period swell waves, due to slow variations in turbine position (mostly due to sway motions).

It is concluded that wind and water tunnel experiments of scaled floating wind farms are possible when geometric scaling of the floaters is relaxed such that the dynamics can be correctly matched (i.e., changes to the turbine platform design allow for relaxing Froude scaling such that the Reynolds number can be kept large enough). These first experiments with appropriately scaled model floating wind turbines confirm distinct impacts of turbine motion on wake recovery and meandering, and highlight the intricate interactions of wave topology, wake meandering and wind farm power production.

ACKNOWLEDGMENTS

J.B. received funding from the Belgian American Educational Foundation. D.G. and C.M. are supported by NSF (Grant No. CMMI 2034111). O.F., Z.S., J.B., and R.B.C. are supported by NSF (Grants No. NSF-CMMI-2034160, No. NSF-CBET-2227263, and No. NSF-CBET-2037582).

APPENDIX A: PARTICLE IMAGE VELOCIMETRY SETUP

Stereoscopic particle image velocimetry (S-PIV) is used to measure two-dimensional-three-component (2-D-3C) velocity fields perpendicular to the main flow direction. The S-PIV set-up consists of two 4M pixel CCD cameras and a Litron Nano double pulsed Nd:YAG (532 nm, 1200 mJ,

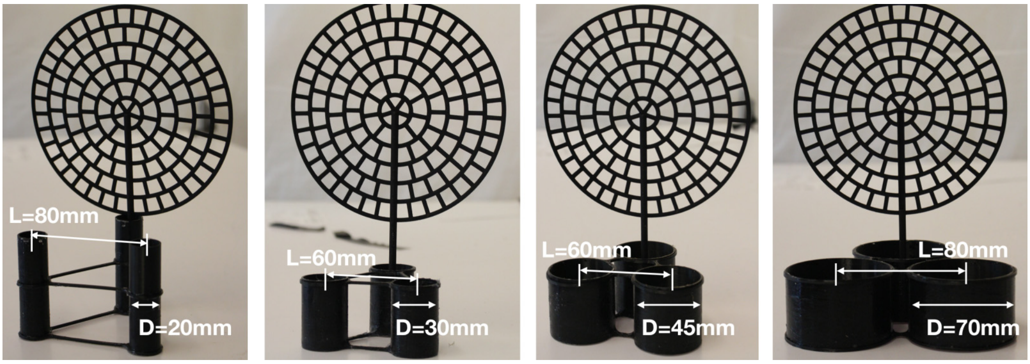

FIG. 27. Dummy floater designs to explore sensitivity of pitch response to floater dimensions and ballast.

4 ns duration) laser. The camera lenses have a focal length of 50 mm. The cameras are oriented at an angle of 40 degrees with the measurement plane, such that they have optical access between two rows of floating turbines, to a cross-plane at a downstream distance of $x/D = 3$ from the center turbine in the third row. The thickness of the laser sheet is approximately 4 mm. The uncertainty on the measured velocities is estimated with Davis 10 software using the correlation statistics approach by Wieneke [101]. The estimated uncertainty over all planes is 0.01 m/s or smaller for all velocity components, which corresponds to 0.2% of the freestream velocity during the tests ($U_0 = 4.1\,\mathrm{m/s}$). The cameras are set up on one side of the wind tunnel. A Scheimpflug adapter is used to correct the camera focus to the measurement plane. Neutrally buoyant fluid particles of diethylhexyl sebacate are aerosolized by a seeding generator with a constant density throughout the experiment. For each case, 5000 independent snapshot-pairs are recorded at a frequency of 3.75 Hz. Davis 10 software is used to apply a multipass Fourier transform-based cross-correlation algorithm and apply a universal outlier detection method to filter out any bad vectors. A multiple-pass reducing size interrogation window of 64×64 pixels and 32×32 pixels, with a 50% overlap is used to process the data. The resulting vector resolution is 2.2 mm. Statistical averaging is performed by averaging over all S-PIV data snapshots. During the PIV measurements, the fluorescence dye helped reduce reflections, and made it possible to identify the water surface following the same approach explained in Sec. III A.

For tests with a single turbine, 2D-2C PIV is used to measure velocity fields in a streamwise aligned plane. The PIV setup consists of a single 4 megapixel CCD camera and the same Litron Nano double pulsed Nd:YAG (532 nm, 1200 mJ, 4 ns duration) laser. The camera lens has a focal length of 50 mm. For each measurement 500 independent image-pairs are recorded at a frequency of 4 Hz, resulting in an estimated standard error of mean velocity smaller than 0.5%. The uncertainty in Davis 10 is estimated as 0.4% of the free-stream velocity for the horizontal velocity, and 0.25% for the vertical velocity component. PIV processing is done in the same way as for the S-PIV measurements. The PIV window covers an area of $0.2\,\mathrm{m}\times 0.2\,\mathrm{m}$, resulting in a vector resolution of 1.9 mm.

APPENDIX B: HYDRODYNAMIC RESPONSE SENSITIVITY TO FLOATER DIMENSIONS

The dependence of the pitch natural frequency to floater dimensions is verified by measuring the response of several different floater designs, as shown in Fig. 27. These measurement results are shown in Table VI, and are performed with an MPU6050 gyro and accelerometer connected to an Arduino Due. The tests are done outside of the wind tunnel, with zero wind speed. The weight of the rotor is represented by a simple porous disk. These tests are only used to make a first evaluation of the required floater dimensions.

TABLE VI. Overview of measured natural frequency of tilt for different dummy floater designs.

Floater diameter [mm]	Floater spacing [mm]	Total mass [g]	Natural frequency for pitch [Hz]
20	80	53	0.9
30	60	55	1.1
30	60	77	1
45	60	46	2
45	60	158	1.85
70	80	105	2.4
70	80	325	2

[1] U.S. Department of the Interior, Biden-Harris administration announces winners of California offshore wind energy auction (2022).

[2] Offshore Wind Ireland, Floating wind in Scotland (2022).

[3] Reuters, Portugal ups debut offshore wind auction target to 10 GW (2022).

[4] U.S. Department of Energy, Floating offshore wind shot (2022).

[5] A. J. Goupee, B. J. Koo, R. W. Kimball, K. F. Lambrakos, and H. J. Dagher, Experimental comparison of three floating wind turbine concepts, J. Offshore Mech. Arct. Eng. **136**, 020906 (2014).

[6] A. R. Henderson, D. Witcher, and C. A. Morgan, Floating support structures enabling new markets for offshore wind energy, in *Proceedings of the European Wind Energy Conference (EWEC)* (WindEurope, Marseille, France, 2009), Vol. 4.

[7] S. Butterfield, W. Musial, J. Jonkman, and P. Sclavounos, Engineering challenges for floating offshore wind turbines, Technical Report, National Renewable Energy Laboratory (NREL), Golden, CO (2007).

[8] A. Cordle and J. Jonkman, State of the art in floating wind turbine design tools, in *Proceedings of the 21st International Offshore and Polar Engineering Conference (OnePetro)* (2011).

[9] S. Chakrabarti, Physical model testing of floating offshore structures, in *Proceedings of the Dynamic Positioning Conference* (Dynamic Positioning Committee of the Marine Technology Society, 1998), Vol. 1, pp. 1–33.

[10] P. Chen, J. Chen, and Z. Hu, Review of experimental-numerical methodologies and challenges for floating offshore wind turbines, J. Marine. Sci. Appl. **19**, 339 (2020).

[11] M. F. Howland, J. Bossuyt, L. A. Martínez-Tossas, J. Meyers, and C. Meneveau, Wake structure in actuator disk models of wind turbines in yaw under uniform inflow conditions, J. Renew. Sustain. Energy **8**, 043301 (2016).

[12] C. Cossu, Evaluation of tilt control for wind-turbine arrays in the atmospheric boundary layer, Wind Energy Sci. **6**, 663 (2021).

[13] J. Bossuyt, R. Scott, N. Ali, and R. B. Cal, Quantification of wake shape modulation and deflection for tilt and yaw misaligned wind turbines, J. Fluid Mech. **917**, A3 (2021).

[14] C. R. Shapiro, D. F. Gayme, and C. Meneveau, Modelling yawed wind turbine wakes: A lifting line approach, J. Fluid Mech. **841**, R1 (2018).

[15] C. R. Shapiro, D. F. Gayme, and C. Meneveau, Generation and decay of counter-rotating vortices downstream of yawed wind turbines in the atmospheric boundary layer, J. Fluid Mech. **903**, R2 (2020).

[16] G. Narasimhan, D. F. Gayme, and C. Meneveau, Effects of wind veer on a yawed wind turbine wake in atmospheric boundary layer flow, Phys. Rev. Fluids **7**, 114609 (2022).

[17] M. Bastankhah, C. R. Shapiro, S. Shamsoddin, D. F. Gayme, and C. Meneveau, A vortex sheet based analytical model of the curled wake behind yawed wind turbines, J. Fluid Mech. **933**, A2 (2022).

[18] C. R. Shapiro, G. M. Starke, C. Meneveau, and D. F. Gayme, A wake modeling paradigm for wind farm design and control, Energies **12**, 2956 (2019).

[19] D. Matha, M. Schlipf, A. Cordle, R. Pereira, and J. Jonkman, Challenges in simulation of aerodynamics, hydrodynamics, and mooring-line dynamics of floating offshore wind turbines, Technical Report, National Renewable Energy Laboratory (NREL), Golden, CO (2011).

[20] S. Rockel, E. Camp, J. Schmidt, J. Peinke, R. B. Cal, and M. Hölling, Experimental study on influence of pitch motion on the wake of a floating wind turbine model, Energies **7**, 1954 (2014).

[21] H. Kadum, S. Rockel, M. Hölling, J. Peinke, and R. B. Cal, Wind turbine wake intermittency dependence on turbulence intensity and pitch motion, J. Renew. Sustain. Energy **11**, 053302 (2019).

[22] R. Scott, J. Bossuyt, and R. B. Cal, Characterizing tilt effects on wind plants, J. Renew. Sustain. Energy **12**, 043302 (2020).

[23] H. Kadum, S. Rockel, B. Viggiano, T. Dib, M. Hölling, L. Chevillard, and R. B. Cal, Assessing intermittency characteristics via cumulant analysis of floating wind turbines wakes, J. Renew. Sustain. Energy **13**, 013302 (2021).

[24] R. Scott, L. Martínez-Tossas, J. Bossuyt, N. Hamilton, and R. B. Cal, Evolution of eddy viscosity in the wake of a wind turbine, Wind Energy Sci. Discuss. **8**, 449 (2022).

[25] T. Messmer, M. Hölling, and J. Peinke, Enhanced recovery and nonlinear dynamics in the wake of a model floating offshore wind turbine submitted to side-to-side and fore-aft motion, arXiv:2305.12247.

[26] G. M. Starke, C. Meneveau, J. King, and D. F. Gayme, Yaw-augmented control for wind farm power tracking, in *Proceedings of the American Control Conference (ACC)* (IEEE, Piscataway, NJ, 2023), pp. 184–191.

[27] T. Sebastian and M. Lackner, Characterization of the unsteady aerodynamics of offshore floating wind turbines, Wind Energy **16**, 339 (2013).

[28] R. Farrugia, T. Sant, and D. Micallef, A study on the aerodynamics of a floating wind turbine rotor, Renew. Energy **86**, 770 (2016).

[29] T. T. Tran and D. H. Kim, The aerodynamic interference effects of a floating offshore wind turbine experiencing platform pitching and yawing motions, J. Mech. Sci. Technol. **29**, 549 (2015).

[30] T. T. Tran and D.-H. Kim, A CFD study into the influence of unsteady aerodynamic interference on wind turbine surge motion, Renew. Energy **90**, 204 (2016).

[31] H. Lee and D.-J. Lee, Effects of platform motions on aerodynamic performance and unsteady wake evolution of a floating offshore wind turbine, Renew. Energy **143**, 9 (2019).

[32] G. Chen, X.-F. Liang, and X.-B. Li, Modelling of wake dynamics and instabilities of a floating horizontal-axis wind turbine under surge motion, Energy **239**, 122110 (2022).

[33] V. G. Kleine, L. Franceschini, B. S. Carmo, A. Hanifi, and D. S. Henningson, The stability of wakes of floating wind turbines, Phys. Fluids **34**, 074106 (2022).

[34] Z. Li, G. Dong, and X. Yang, Onset of wake meandering for a floating offshore wind turbine under side-to-side motion, J. Fluid Mech. **934**, A29 (2022).

[35] N. Ramos-García, S. Kontos, A. Pegalajar-Jurado, S. González Horcas, and H. Bredmose, Investigation of the floating IEA wind 15 MW RWT using vortex methods. Part I: Flow regimes and wake recovery, Wind Energy **25**, 468 (2022).

[36] R. Farrugia, T. Sant, and D. Micallef, Investigating the aerodynamic performance of a model offshore floating wind turbine, Renew. Energy **70**, 24 (2014).

[37] T. Sant, D. Bonnici, R. Farrugia, and D. Micallef, Measurements and modelling of the power performance of a model floating wind turbine under controlled conditions, Wind Energy **18**, 811 (2015).

[38] I. Bayati, M. Belloli, L. Bernini, and A. Zasso, Wind tunnel wake measurements of floating offshore wind turbines, Energy Procedia **137**, 214 (2017).

[39] S. Fu, Y. Jin, Y. Zheng, and L. P. Chamorro, Wake and power fluctuations of a model wind turbine subjected to pitch and roll oscillations, Appl. Energy **253**, 113605 (2019).

[40] B. Schliffke, S. Aubrun, and B. Conan, Wind tunnel study of a “floating” wind turbine’s wake in an atmospheric boundary layer with imposed characteristic surge motion, in *Journal of Physics: Conference Series* (IOP Publishing, Bristol, UK, 2020), Vol. 1618, p. 062015.

[41] K. M. Kopperstad, R. Kumar, and K. Shoele, Aerodynamic characterization of barge and spar type floating offshore wind turbines at different sea states, Wind Energy **23**, 2087 (2020).

[42] A. Fontanella, I. Bayati, R. Mikkelsen, M. Belloli, and A. Zasso, Unaflow: A holistic wind tunnel experiment about the aerodynamic response of floating wind turbines under imposed surge motion, Wind Energy Sci. **6**, 1169 (2021).

[43] N. Belvasi, B. Conan, B. Schliffke, L. Perret, C. Desmond, J. Murphy, and S. Aubrun, Far-wake meandering of a wind turbine model with imposed motions: An experimental s-piv analysis, Energies **15**, 7757 (2022).

[44] A. Fontanella, A. Zasso, and M. Belloli, Wind tunnel investigation of the wake-flow response for a floating turbine subjected to surge motion, in *Journal of Physics: Conference Series*, Vol. 2265 (IOP Publishing, Bristol, UK, 2022), p. 042023.

[45] H. Meng, H. Su, T. Qu, and L. Lei, Wind tunnel study on the wake characteristics of a wind turbine model subjected to surge and sway motions, J. Renew. Sustain. Energy **14**, 013307 (2022).

[46] R. B. Cal, J. Lebrón, L. Castillo, H. S. Kang, and C. Meneveau, Experimental study of the horizontally averaged flow structure in a model wind-turbine array boundary layer, J. Renew. Sustain. Energy **2**, 013106 (2010).

[47] M. Calaf, C. Meneveau, and J. Meyers, Large eddy simulation study of fully developed wind-turbine array boundary layers, Phys. Fluids **22**, 015110 (2010).

[48] N. Hamilton, H. Suk Kang, C. Meneveau, and R. Bayoán Cal, Statistical analysis of kinetic energy entrainment in a model wind turbine array boundary layer, J. Renew. Sustain. Energy **4**, 063105 (2012).

[49] J. Bossuyt, C. Meneveau, and J. Meyers, Effect of layout on asymptotic boundary layer regime in deep wind farms, Phys. Rev. Fluids **3**, 124603 (2018).

[50] J. Bossuyt, M. Howland, C. Meneveau, and J. Meyers, Measuring power output intermittency and unsteady loading in a micro wind farm model, in *Proceedings of the 34th Wind Energy Symposium* (AIAA Press, Reston, VA, 2016), p. 1992.

[51] E. H. Camp and R. B. Cal, Low-dimensional representations and anisotropy of model rotor versus porous disk wind turbine arrays, Phys. Rev. Fluids **4**, 024610 (2019).

[52] N. Hamilton, B. Viggiano, M. Calaf, M. Tutkun, and R. B. Cal, A generalized framework for reduced-order modeling of a wind turbine wake, Wind Energy **21**, 373 (2018).

[53] G. Cortina, M. Calaf, and R. B. Cal, Distribution of mean kinetic energy around an isolated wind turbine and a characteristic wind turbine of a very large wind farm, Phys. Rev. Fluids **1**, 074402 (2016).

[54] E. H. Camp and R. B. Cal, Mean kinetic energy transport and event classification in a model wind turbine array versus an array of porous disks: Energy budget and octant analysis, Phys. Rev. Fluids **1**, 044404 (2016).

[55] Z. Sadek, R. Scott, N. Hamilton, and R. B. Cal, A three-dimensional, analytical wind turbine wake model: Flow acceleration, empirical correlations, and continuity, Renew. Energy **209**, 298 (2023).

[56] S. E. Smith, K. N. Travis, H. Djeridi, M. Obligado, and R. B. Cal, Dynamic effects of inertial particles on the wake recovery of a model wind turbine, Renew. Energy **164**, 346 (2021).

[57] R. Scott, B. Viggiano, T. Dib, N. Ali, M. Hölling, J. Peinke, and R. B. Cal, Wind turbine partial wake merging description and quantification, Wind Energy **23**, 1610 (2020).

[58] N. Ali and R. B. Cal, Data-driven modeling of the wake behind a wind turbine array, J. Renew. Sustain. Energy **12**, 033304 (2020).

[59] D. Yang, C. Meneveau, and L. Shen, Large-eddy simulation of offshore wind farm, Phys. Fluids **26**, 025101 (2014).

[60] O. Ferčák, J. Bossuyt, N. Ali, and R. B. Cal, Decoupling wind-wave-wake interactions in a fixed-bottom offshore wind turbine, Appl. Energy **309**, 118358 (2022).

[61] H. Yang, M. Ge, M. Abkar, and X. I. Yang, Large-eddy simulation study of wind turbine array above swell sea, Energy **256**, 124674 (2022).

[62] T. Hegberg, G. Corten, and P. Schaak, Turbine interaction in large offshore wind farms. wind tunnel measurements (2004).

[63] L. P. Chamorro, R. E. Arndt, and F. Sotiropoulos, Reynolds number dependence of turbulence statistics in the wake of wind turbines, Wind Energy **15**, 733 (2012).

[64] M. Bastankhah and F. Porté-Agel, A new miniature wind turbine for wind tunnel experiments. Part I: Design and performance, Energies **10**, 908 (2017).

[65] S. A. Hughes, *Physical Models and Laboratory Techniques in Coastal Engineering* (World Scientific, Singapore, 1993), Vol. 7.

[66] V. Heller, Scale effects in physical hydraulic engineering models, J. Hydraul. Res. **49**, 293 (2011).

[67] J. Jonkman, S. Butterfield, W. Musial, and G. Scott, Definition of a 5-MW reference wind turbine for offshore system development, Technical Report, National Renewable Energy Laboratory (NREL), Golden, CO (2009).

[68] G. Stewart and M. Muskulus, A review and comparison of floating offshore wind turbine model experiments, Energy Procedia **94**, 227 (2016).

[69] M. A. Miller, J. Kiefer, C. Westergaard, M. O. L. Hansen, and M. Hultmark, Horizontal axis wind turbine testing at high Reynolds numbers, Phys. Rev. Fluids **4**, 110504 (2019).

[70] M. J. Fowler, R. W. Kimball, D. A. Thomas III, and A. J. Goupee, Design and testing of scale model wind turbines for use in wind/wave basin model tests of floating offshore wind turbines, in *Proceedings of the International Conference on Offshore Mechanics and Arctic Engineering* (American Society of Mechanical Engineers, New York, NY, 2013), Vol. 55423, p. V008T09A004.

[71] A. Otter, J. Murphy, V. Pakrashi, A. Robertson, and C. Desmond, A review of modelling techniques for floating offshore wind turbines, Wind Energy **25**, 831 (2022).

[72] L. P. Chamorro and F. Porté-Agel, Turbulent flow inside and above a wind farm: A wind-tunnel study, Energies **4**, 1916 (2011).

[73] W. Zhang, C. D. Markfort, and F. Porté-Agel, Wind-turbine wakes in a convective boundary layer: A wind-tunnel study, Boundary-Layer Meteorol. **146**, 161 (2013).

[74] H. C. Lim, I. P. Castro, and R. P. Hoxey, Bluff bodies in deep turbulent boundary layers: Reynolds-number issues, J. Fluid Mech. **571**, 97 (2007).

[75] A. N. Robertson, F. Wendt, J. M. Jonkman, W. Popko, H. Dagher, S. Gueydon, J. Qvist, F. Vittori, J. Azcona, E. Uzunoglu *et al.*, Oc5 project phase II: Validation of global loads of the deepcwind floating semisubmersible wind turbine, Energy Procedia **137**, 38 (2017).

[76] D. Marten, Doctoral Thesis, Qblade: A modern tool for the aeroelastic simulation of wind turbines, 2020.

[77] H. R. Martin, Master Thesis, Development of a scale model wind turbine for testing of offshore floating wind turbine systems, 2011.

[78] M. P. Buckley and F. Veron, The turbulent airflow over wind generated surface waves, Eur. J. Mech. B Fluids **73**, 132 (2019).

[79] N. Machicoane, A. Aliseda, R. Volk, and M. Bourgoin, A simplified and versatile calibration method for multi-camera optical systems in 3D particle imaging, Rev. Sci. Instrum. **90**, 035112 (2019).

[80] N. Hamilton, M. Melius, and R. B. Cal, Wind turbine boundary layer arrays for cartesian and staggered configurations. Part I, flow field and power measurements, Wind Energy **18**, 277 (2015).

[81] A. S. Aseyev and R. B. Cal, Vortex identification in the wake of a model wind turbine array, J. Turbul. **17**, 357 (2016).

[82] N. Ali, N. Hamilton, D. DeLucia, and R. Bayoán Cal, Assessing spacing impact on coherent features in a wind turbine array boundary layer, Wind Energy Sci. **3**, 43 (2018).

[83] Y. Odemark and J. H. Fransson, The stability and development of tip and root vortices behind a model wind turbine, Exp. Fluids **54**, 1591 (2013).

[84] A. J. Coulling, A. J. Goupee, A. N. Robertson, J. M. Jonkman, and H. J. Dagher, Validation of a fast semisubmersible floating wind turbine numerical model with deepcwind test data, J. Renew. Sustain. Energy **5**, 023116 (2013).

[85] J. Azcona, F. Bouchotrouch, M. González, J. Garciandía, X. Munduate, F. Kelberlau, and T. A. Nygaard, Aerodynamic thrust modelling in wave tank tests of offshore floating wind turbines using a ducted fan, in *Journal of Physics: Conference Series* (IOP Publishing, Bristol, UK, 2014), Vol. 524, p. 012089.

[86] M. T. Hall, Hybrid modeling of floating wind turbines, Ph.D. thesis, University of Maine, 2016.

[87] A. N. Robertson, J. M. Jonkman, A. J. Goupee, A. J. Coulling, I. Prowell, J. Browning, M. D. Masciola, and P. Molta, Summary of conclusions and recommendations drawn from the deepcwind scaled floating offshore wind system test campaign, in *Proceedings of the International Conference on Offshore Mechanics and Arctic Engineering* (American Society of Mechanical Engineers, New York, NY, 2013), Vol. 55423, p. V008T09A053.

[88] L. Li, Y. Gao, Z. Hu, Z. Yuan, S. Day, and H. Li, Model test research of a semisubmersible floating wind turbine with an improved deficient thrust force correction approach, Renew. Energy **119**, 95 (2018).

[89] S. Gueydon, Aerodynamic damping on a semisubmersible floating foundation for wind turbines, Energy Procedia **94**, 367 (2016).

[90] E. E. Bachynski, M. Etemaddar, M. I. Kvittem, C. Luan, and T. Moan, Dynamic analysis of floating wind turbines during pitch actuator fault, grid loss, and shutdown, Energy Procedia **35**, 210 (2013).

[91] A. J. Goupee, M. J. Fowler, R. W. Kimball, J. Helder, and E.-J. de Ridder, Additional wind/wave basin testing of the deepcwind semisubmersible with a performance-matched wind turbine, in *Proceedings of the International Conference on Offshore Mechanics and Arctic Engineering* (American Society of Mechanical Engineers, New York, NY, 2014), Vol. 45547, p. V09BT09A026.

[92] J. Lighthill, *Waves in Fluids* (Cambridge University Press, Cambridge, UK, 2001).

[93] C. D. Markfort, W. Zhang, and F. Porté-Agel, Analytical model for mean flow and fluxes of momentum and energy in very large wind farms, Boundary-Layer Meteorol. **166**, 31 (2018).

[94] N. G. Nygaard, Wakes in very large wind farms and the effect of neighbouring wind farms, in *Journal of Physics: Conference Series* (IOP Publishing, Bristol, UK, 2014), Vol. 524, p. 012162.

[95] J. Bossuyt, M. F. Howland, C. Meneveau, and J. Meyers, Measurement of unsteady loading and power output variability in a micro wind farm model in a wind tunnel, Exp. Fluids **58**, 1 (2017).

[96] M. Hall and A. Goupee, Validation of a lumped-mass mooring line model with deepcwind semisubmersible model test data, Ocean Eng. **104**, 590 (2015).

[97] B. Skaare, F. G. Nielsen, T. D. Hanson, R. Yttervik, O. Havmøller, and A. Rekdal, Analysis of measurements and simulations from the hywind demo floating wind turbine, Wind Energy **18**, 1105 (2015).

[98] I. Marusic, Evidence of very long meandering features in the logarithmic region of turbulent boundary layers, J. Fluid Mech. **579**, 1 (2007).

[99] L. J. Lukassen, R. J. Stevens, C. Meneveau, and M. Wilczek, Modeling space-time correlations of velocity fluctuations in wind farms, Wind Energy **21**, 474 (2018).

[100] J. Bossuyt, C. Meneveau, and J. Meyers, Wind farm power fluctuations and spatial sampling of turbulent boundary layers, J. Fluid Mech. **823**, 329 (2017).

[101] B. Wieneke, Piv uncertainty quantification from correlation statistics, Meas. Sci. Technol. **26**, 074002 (2015).